

# Superconducting states and depinning transitions of Josephson ladders

Mauricio Barahona\*

*Physics Department, Massachusetts Institute of Technology, Cambridge, MA 02139*

Steven H. Strogatz

*Kimball Hall, Department of Theoretical and Applied Mechanics and Center for Applied Mathematics, Cornell University, Ithaca, NY 14853*

Terry P. Orlando

*Department of Electrical Engineering and Computer Science, Massachusetts Institute of Technology, Cambridge, MA 02139*

(To appear in Phys. Rev. B, Jan 1 1998)

We present analytical and numerical studies of pinned superconducting states of open-ended Josephson ladder arrays, neglecting inductances but taking edge effects into account. Treating the edge effects perturbatively, we find analytical approximations for three of these superconducting states – the no-vortex, fully-frustrated and single-vortex states – as functions of the dc bias current  $I$  and the frustration  $f$ . Bifurcation theory is used to derive formulas for the depinning currents and critical frustrations at which the superconducting states disappear or lose dynamical stability as  $I$  and  $f$  are varied. These results are combined to yield a zero-temperature stability diagram of the system with respect to  $I$  and  $f$ . To highlight the effects of the edges, we compare this dynamical stability diagram to the thermodynamic phase diagram for the infinite system where edges have been neglected. We briefly indicate how to extend our methods to include self-inductances.

PACS Numbers: 74.50.+r, 05.45.+b, 74.40.+k

## I. INTRODUCTION

Arrays of Josephson junctions are of interest in several branches of physics<sup>1</sup>. They have many technological applications, including high-frequency emitters and detectors, parametric amplifiers, local oscillators, and voltage standards<sup>1,2</sup>. They also shed light on the structural<sup>3</sup> and pinning<sup>4</sup> properties of the high- $T_c$  superconducting cuprates. At the same time, they provide model systems for the study of problems in both spatiotemporal nonlinear dynamics<sup>5–8</sup> and nonequilibrium statistical physics<sup>8,9</sup>. For instance, the depinning transitions and nonlinear wave propagation seen in Josephson arrays are analogous to those found in incommensurate systems, earthquake models, Type II superconductors, and charge-density waves.

From the standpoint of dynamical systems theory<sup>10</sup>, Josephson arrays can be viewed as large collections of coupled nonlinear oscillators. Unfortunately, because of their nonlinearity and large number of degrees of freedom, these arrays are inherently difficult to analyze mathematically. A further complication is that there is an intrinsic physical coupling among junctions, due to fluxoid quantization, which is more awkward to handle than the nearest-neighbor interaction usually assumed in idealized models of coupled oscillators. And when the effects of self-fields and inductances are included, there is even less hope of making analytical progress.

Despite these obstacles, some encouraging advances have occurred recently in the mathematical analysis of Josephson arrays, especially for one-dimensional (1-D) systems where the junctions are connected in series<sup>5,6</sup> or in parallel<sup>7</sup>. The logical next step is to tackle two-dimensional (2-D) arrays. Much of the previous theoretical work on 2-D arrays has focused on numerical simulation of the current-voltage characteristics<sup>11</sup>, in an effort to link the rich spatiotemporal dynamics of 2-D arrays to the averaged quantities that are most readily measured experimentally. On the mathematical side, there are recent indications that 2-D arrays, like their 1-D counterparts, are also going to be tractable in some regimes<sup>12</sup>.

An ideal example to explore the crossover between 1-D and 2-D behavior is the Josephson ladder array (Figure 1). Following Kardar<sup>13,14</sup>, several authors have studied various statistical properties of the frustrated ladder, including its ground state, the complicated landscape of solutions at zero temperature, the low-lying excitations, and the linear response regime<sup>15–17</sup>. However, all of these authors restricted attention to ladders in the absence of a driving current. Only recently has the fully dynamical problem been addressed, through numerical simulations of the depinning transition<sup>18</sup> and vortex propagation<sup>19</sup>.

In this paper we use the tools of nonlinear dynamics to analyze the superconducting states of ladder arrays. (Other dynamical regimes will be discussed elsewhere<sup>20,21</sup>.) Mathematically, the superconducting states correspond to fixed points of the governing circuit equations. We study the bifurcations of these fixed points with respect to variations in the applied dc bias current

---

\*Present address: Ginzton Laboratory, Stanford University, Stanford, CA 94305.

$I$  and the frustration  $f$  introduced by an external magnetic field. As  $I$  is increased from 0 at fixed  $f$ , we find that the stable superconducting states are destroyed in saddle-node bifurcations at certain critical values of the current. Then the system depins from its original static configuration and evolves toward some other state. The new state might be another fixed point, or it might be a running solution, in which case a nonzero dc voltage appears across the array. Global depinning of the array occurs when the last stable fixed point is destroyed. One of the main results of our analysis is a set of approximate analytical formulas for the critical currents at which the fixed points are destroyed, as a function of  $f$ , for the three most important types of superconducting states: the no-vortex, fully-frustrated and single-vortex solutions.

Another important finding is that symmetry plays a crucial role in the dynamics of the ladder. As we will show below, much of the behavior of the ladder can be understood by focusing on states that are “up-down symmetric” – in other words, states where the phases of the horizontal junctions on the top and bottom of any given plaquette are equal in magnitude but opposite in sign at all times. All of the stable superconducting states possess this symmetry. Even when the parameters are chosen so that depinning occurs, the subsequent transients and long-term running solutions typically remain up-down symmetric. But there is at least one exception: when the single-vortex state is destabilized by lowering the frustration  $f$  below some critical value  $f_{\min}$ , the system depins via a symmetry-breaking bifurcation. During the transient behavior, the up-down symmetry is lost temporarily, but is then recovered as the system expels flux from the array and evolves toward the no-vortex state.

These symmetry considerations establish an unexpected link between the study of Josephson arrays and some recent developments in nonlinear dynamics. In mathematical terms, the up-down symmetric states of a ladder array form an invariant manifold of the full state space. A symmetry-breaking bifurcation occurs when this manifold loses stability in a transverse direction. The same issue – the transverse stability of an invariant manifold – arises in the study of riddled basins, synchronized chaos, on-off intermittency, and blowout bifurcations<sup>22</sup>. These connections suggest a promising line of future research on Josephson arrays, particularly with regard to their chaotic states.

We will also show that the dynamics of ladder arrays are very strongly influenced by edge effects. One might have supposed these effects to be negligible, especially in long ladders, since their influence on the superconducting solutions dies off exponentially fast away from the boundaries. Yet although the edges do indeed have a small effect on the *form* of the superconducting solutions, they have a large effect on the *stability* of those solutions. Much of this paper is devoted to investigating the effects of the edges, first on the superconducting states them-

selves, then on their stability, and finally on the entire phase diagram.

This paper is organized as follows. Section II reviews the model equations for the ladder and discusses their symmetry properties. In Section III we obtain analytical approximations for three numerically observed superconducting solutions: the no-vortex (nv), single-vortex (sv), and fully-frustrated (ff) solutions. In all cases, edge effects are taken into account via perturbation theory. Next, in Section IV we describe the dynamical simulations which reveal the depinning properties of the nv, sv, and ff configurations and relate them to the global depinning of the ladder. In Section V we establish the rigorous connection of the dynamical depinning with the stability of these three fixed points. For all of them, we characterize the bifurcations and study their stability diagrams, both in the presence and in the absence of edges. When possible, analytical approximations to the critical currents are obtained. We show that the depinning transitions correspond to saddle-node bifurcations that are edge-dominated for almost all values of the frustration. Moreover, we find that some of the superconducting states can be destabilized via a subcritical pitchfork bifurcation as the frustration is reduced; in physical terms, this is a symmetry-breaking bifurcation in which flux is expelled *transversally* from the ladder. In the final section we summarize our conclusions in two phase diagrams (for ladders with and without edges), and we relate our results to those found by previous authors. We also add two more technical appendices: Appendix A compares the single-vortex configuration in the ladder with the corresponding kink-like solution in 1-D parallel arrays; Appendix B briefly indicates how to extend our approach to include self-inductance effects.

## II. THE SYSTEM

We study an open-ended Josephson ladder with  $N$  square plaquettes, i.e., an array formed by two rows of  $N+1$  weakly coupled superconducting islands (Figure 1). The array is driven by a perpendicular uniform dc current  $I$ , and a magnetic field is applied transverse to the plane of the device. Each weak link between islands constitutes a junction. Its state is described by the gauge-invariant phase difference  $\phi_j$ , arising from the macroscopic character of the quantum wavefunction of the superconductors.

Assuming zero temperature, negligible charging (quantum) effects, and identical junctions, the dynamics of each junction is given, in the three-channel RCSJ model<sup>1</sup>, by the nonlinear differential equation

$$I_j = \ddot{\phi}_j + \beta_c^{-1/2} \dot{\phi}_j + \sin \phi_j \equiv \mathcal{N}(\phi_j). \quad (1)$$

Here  $\beta_c$  is the McCumber parameter<sup>1</sup>;  $I_j$  is given in units of the critical current of each (identical) junction; derivatives are with respect to time normalized in units of  $\omega_j^{-1}$ , the inverse of the plasma frequency; and  $\mathcal{N}$  is

shorthand for the nonlinear differential operator defined by (1). Thus, each junction is formally equivalent to a damped driven pendulum<sup>10</sup>.

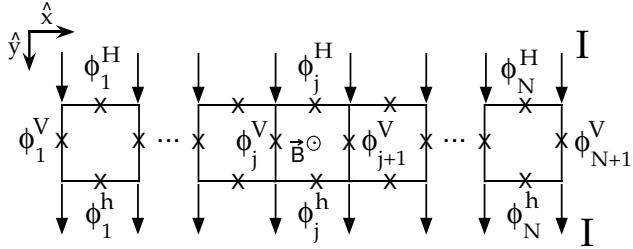


FIG. 1. Schematic diagram of the Josephson ladder array with dc current  $I$  injected in the perpendicular ( $\hat{y}$ ) direction. The external magnetic field  $\mathbf{B}$  is applied transversely to the plane of the device, in the  $-\hat{z}$  direction.

The junctions are *intrinsically* coupled, even when inductances are neglected, through two physical restrictions: the quantization of the magnetic flux through each plaquette, and Kirchhoff's current conservation law at each node. When all inductances are zero, i.e., self-fields are neglected, the flux quantization condition for the array in Figure 1 becomes

$$\phi_j^V + \phi_j^h - \phi_{j+1}^V - \phi_j^H = 2\pi(n_j - f), \quad j = 1, \dots, N \quad (2)$$

where  $f$  is the *external* magnetic flux in units of the flux quantum  $\Phi_0$ . The set of integers  $\{n_j\}$  indicate the presence ( $n_j = \pm 1$ ) or absence ( $n_j = 0$ ) of topological vortices in each plaquette when the phases are restricted to the interval  $[-\pi, \pi]$ .

In addition, Kirchhoff's current law yields

$$I_{j-1}^H + I = I_j^H + I_j^V, \quad j = 2, \dots, N \quad (3)$$

$$I_{j-1}^h + I_j^V = I + I_j^h, \quad j = 2, \dots, N \quad (4)$$

at the interior nodes of the ladder. At the left edge,

$$I = I_1^H + I_1^V, \quad (5)$$

$$I_1^V = I + I_1^h, \quad (6)$$

while at the right edge,

$$I_N^H + I = I_{N+1}^V, \quad (7)$$

$$I_{N+1}^V + I_N^h = I. \quad (8)$$

In summary, equations (1)–(8) define our model for the dynamics of the ladder array. A useful mechanical analog

for the system is a frustrated lattice of coupled, damped, nonlinear pendula driven by a constant torque applied at the edges.

An important restriction on the currents immediately follows from the presence of the edges. Equations (5) and (6) imply that  $I_1^H = -I_1^h$ . Moving successively from the left edge to the interior of the ladder, Kirchhoff's current law yields

$$I_j^H = -I_j^h, \quad \forall j. \quad (9)$$

This condition (9) is automatically satisfied by any phase configuration whose evolution obeys the *up-down symmetry*

$$\phi_j^H(t) = -\phi_j^h(t), \quad \forall j, \forall t \quad (10)$$

as can be seen from (1). Moreover, if the initial conditions satisfy  $\phi_j^H(0) = -\phi_j^h(0)$  along with similar equalities on the first time-derivatives, the governing equations imply that those equalities will hold for *all* time. In geometrical terms, the set of all up-down symmetric states (10) forms an invariant submanifold of the full phase space.

On the other hand, it is certainly possible to choose initial conditions that do not have this up-down symmetry. But our simulations indicate that for a wide range of parameters and initial conditions, arbitrary phase configurations rapidly evolve toward up-down symmetric states. In other words, the invariant manifold is typically attracting in the transverse directions — initial states that are off the manifold are soon drawn onto it. There are also exceptions to this rule: as we will see in Section V, the single-vortex and fully-frustrated states can lose transverse stability as the frustration  $f$  decreases. Nevertheless, a great deal of insight can be obtained by restricting attention to the submanifold of up-down symmetric states. Thus, for much of this paper we will assume that (10) holds, and we will replace  $\phi_j^h$  with  $-\phi_j^H$  throughout the governing equations.

There is a simple condition for the transverse stability of an up-down symmetric fixed point. It can be shown<sup>20</sup> that such a fixed point is linearly stable to perturbations that are *strictly normal* to the manifold if and only if

$$|\phi_j^H| < \pi/2, \quad \forall j. \quad (11)$$

We have checked numerically that in the instances when the up-down symmetry is broken (and, thus, the system escapes the symmetric manifold), the subsequent evolution does in fact take place purely along the normal direction. Therefore, any up-down symmetric fixed point that is stable must satisfy this inequality (11). Hence (11) constitutes a *necessary* condition for stability. (It is not sufficient, however, because it only governs the transverse direction; it says nothing about the stability with respect to perturbations that preserve the symmetry. Further conditions would be needed to ensure stability in directions *along* the invariant manifold as will be shown below.)

In summary, the governing equations can be written compactly as  $\mathbf{f}(\mathbf{x}) = \mathbf{0}$ , with  $\mathbf{x} = (\phi_1^V, \dots, \phi_{N+1}^V, \phi_1^H, \dots, \phi_N^H, \phi_1^h, \dots, \phi_N^h)$ , and with the components of  $\mathbf{f}(\mathbf{x})$  defined by

$$f_j(\mathbf{x}) = I + \mathcal{N}(\phi_{j-1}^H) - \mathcal{N}(\phi_j^H) - \mathcal{N}(\phi_j^V), \quad j = 1, \dots, N+1 \quad (12)$$

$$f_{N+1+j}(\mathbf{x}) = \mathcal{N}(\phi_j^H) + \mathcal{N}(\phi_j^h), \quad j = 1, \dots, N \quad (13)$$

$$f_{2N+1+j}(\mathbf{x}) = \phi_j^V + \phi_j^h - \phi_{j+1}^V - \phi_j^H - 2\pi(n_j - f), \quad j = 1, \dots, N. \quad (14)$$

The dynamical evolution of the state  $\{\mathbf{x}(t), \dot{\mathbf{x}}(t)\}$  of the system is obtained by numerically solving this system of coupled differential and algebraic equations. The dynamics also depend implicitly on the parameters  $I$ ,  $\beta_c$ ,  $f$ , and  $N$ .

In experiments, the most convenient way to probe the dynamics of the array is to measure its dc current-voltage (*IV*) characteristics. From the Josephson relations<sup>1</sup>, the time-dependent voltage across each junction is directly proportional to  $\dot{\phi}_j$ , the time-derivative of its phase. Hence, the total dc voltage  $V$  across the array in the vertical direction is proportional to the spatial *and* temporal average of all the phase derivatives. Although because of this averaging a great deal of dynamical information is lost about the spatiotemporal state of the system, the *IV* curve still provides a useful (if somewhat coarse) indicator of changes in the underlying dynamics as the drive current  $I$  is varied.

In the case of ladder arrays, the *IV* curves display three regions associated with distinct dynamical behaviors<sup>19,20</sup>. At low  $I$ , the system is *superconducting* ( $V = 0$ ) with pinned or slightly oscillating junctions (in the mechanical analog, the pendula are at rest or librating slightly). At a depinning current  $I_{\text{dep}}$ , the array jumps to the *flux-flow* region, in which a finite voltage is produced by vortices of magnetic flux moving across the array. At still higher currents, the dynamics is characterized by *whirling modes*<sup>7</sup> (in the mechanical analog, all the pendula rotate over the top at a nearly uniform angular velocity proportional to the applied torque). In this state, there is a linear *ohmic* dependence of  $V$  on  $I$ . In the remainder of the article we focus on the superconducting states and the critical current  $I_{\text{dep}}$  at which depinning occurs.

### III. OBSERVED SUPERCONDUCTING SOLUTIONS AND ANALYTICAL APPROXIMATIONS

We have performed dynamical simulations of the array in which the current is ramped up from zero with different initial conditions. The superconducting solutions observed in those simulations are always static states, i.e., fixed points of the system. (In principle, time-dependent

solutions with high cancelling symmetry could also have zero total dc voltage, but we never see such states in our simulations.) More specifically, for any given  $\beta_c$  and  $N$ , only three types of configurations appear in the numerics: *no-vortex* solutions (Figure 2) for  $f$  smaller than  $\sim 0.3$ , and solutions of the *single-vortex* type (Figure 3) and *fully-frustrated* type (Figure 4) for  $f \rightarrow 1/2$ . Far from the edges, the no-vortex (nv) state is characterized by identical phases for all junctions. The same applies to the single-vortex (sv) configuration far from both the edges and the center of the vortex. On the other hand, the fully-frustrated (ff) state has a spatial oscillatory pattern with a wavelength equal to two plaquettes. All of these states are modified by noticeable edge effects. Although there are many other static solutions of the system, our numerical simulations indicate that the no-vortex, single-vortex, and fully-frustrated states are the only ones needed to explain the depinning behavior of the array.

When dealing with *fixed points* with up-down symmetry (10) the defining equations (12)–(14) become

$$I + \sin \phi_{j-1}^H = \sin \phi_j^H + \sin \phi_j^V, \quad j = 1, \dots, N+1 \quad (15)$$

$$\phi_j^V - \phi_{j+1}^V - 2\phi_j^H = 2\pi(n_j - f), \quad j = 1, \dots, N \quad (16)$$

where we have defined artificial phases  $\phi_0^H = \phi_{N+1}^H = 0$ . Note that the McCumber parameter  $\beta_c$  does not appear in the equations for the fixed points, and hence does not affect their existence. This is consistent with the numerically observed independence of the depinning behavior on  $\beta_c$ .

In the rest of this section we obtain analytical approximations for the nv, sv, and ff configurations mentioned above. We follow a common scheme for all of them. First, we obtain a no-edge approximation (denoted with a dagger  $\dagger$ ) for the infinite ladder. Second, we introduce the effect of the edges perturbatively to obtain an edge-corrected approximation (identified by a double dagger  $\ddagger$ ). The calculated configurations have been exhaustively compared with the results of numerical simulations with excellent agreement.

#### A. No-vortex solution

Figure 2 (a)–(b) shows a plot of the no-vortex solution, as computed numerically, along with the analytical approximation described below. This state is characterized by the absence of topological vortices ( $n_j = n_{j+1} = 0, \forall j$ ) and, far from the edges, by the constancy of the phases.

As a first approximation, let  $\{\phi_j^{V\dagger}, \phi_j^{H\dagger}\}$  denote the phases of the no-vortex solution for the *infinite* ladder, i.e., in the absence of edge effects. To ease the notation, let  $\phi^{H\dagger}$  denote the common phase of the horizontal junctions (so  $\phi_j^{H\dagger} = \phi^{H\dagger}$  for all  $j$ ), and define  $\phi^{V\dagger}$  similarly

for the phases of the vertical junctions. The only physically acceptable solution of equations (15)–(16) that also satisfies the stability condition (11) is:

$$\phi^{V\dagger} = \arcsin I, \quad \phi^{H\dagger} = \pi f, \quad (17)$$

where  $0 \leq f \leq 1/2$  and all the angles are restricted to the first quadrant.

This solution exists if and only if  $I \leq 1$ . A linear stability analysis shows that, for all  $I < 1$ , the solution is stable if  $\phi^{V\dagger} = \arcsin I \in [0, \pi/2]$ . The other possible solutions with  $\phi^{V\dagger} = \pi - \arcsin I$  or  $\phi^{H\dagger} = \pi f - \pi$  are linearly unstable<sup>20</sup>. In summary, when the edges are completely neglected, the array behaves like a single junction: its only stable no-vortex solution of the observed form (17) disappears at  $I = 1$  through a saddle-node bifurcation. This existence criterion will be used in Section V when discussing the stability properties of the nv solution.

Figure 2 shows that this infinite-ladder approximation works well near the center of the ladder, but breaks down close to the edges. We now take edge effects into account by considering an edge-corrected solution (denoted by  $\ddagger$ )

$$\phi_j^{V\dagger} = \phi^{V\dagger} + A_j, \quad \phi_j^{H\dagger} = \phi^{H\dagger} - B_j. \quad (18)$$

where  $\{A_j, B_j\}$  denote the corrections. From the fixed point equations (15), (16), the  $\{A_j, B_j\}$  must satisfy

$$I + \sin(\pi f - B_{j-1}) = \sin(\pi f - B_j) + \sin(\arcsin I + A_j) \quad (19)$$

$$A_j - A_{j+1} + 2B_j = 0. \quad (20)$$

The corrections  $\{A_j, B_j\}$  are expected to be small, except in a region very close to the edges. Thus, Equation (19) can be expanded to first order in  $A_j$  and  $B_j$  to obtain a second-order difference equation for  $A_j$ :

$$A_{j+1} - 2\alpha A_j + A_{j-1} = 0 \quad (21)$$

$$\text{with } \alpha = 1 + \frac{\sqrt{1 - I^2}}{\cos \pi f}, \quad (22)$$

from which the horizontal corrections are

$$B_j = \frac{A_{j+1} - A_j}{2}. \quad (23)$$

The general solution of (21) is

$$A_j = Pr^{j-(N+1)} + Qr^{1-j} \quad (24)$$

$$\text{where } r = \alpha + \sqrt{\alpha^2 - 1} \equiv e^{1/\lambda}. \quad (25)$$

Hence, the edges produce corrections that decay exponentially from both ends with a characteristic length  $\lambda(I, f)$ . This  $\lambda = 1/\ln r$  is a measure of how small perturbations decay inside of a region with the no-vortex superconducting solution. A similar result was recently obtained by Denniston and Tang<sup>17</sup> using the transfer matrix method for the particular  $I = 0$  case.

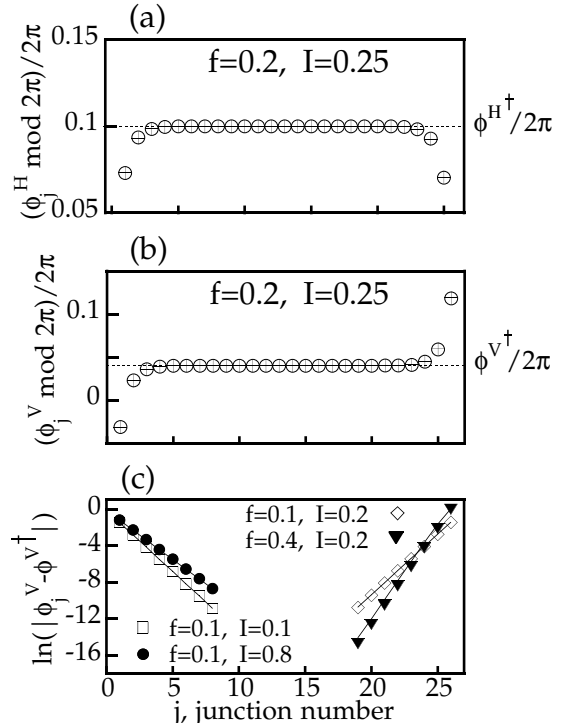


FIG. 2. No-vortex superconducting solution. (a) Phases of the horizontal junctions for a  $25 \times 1$  array with  $I = 0.25$  and  $f = 0.2$ : numerically observed solution (+), and approximate solution  $\phi_j^H \ddagger$  (o). (b) Same as in (a) for the vertical junctions. The predicted phases of the infinite-ladder solution  $\{\phi_j^V \ddagger, \phi_j^H \ddagger\}$  (short-dashed line) are seen to be valid far from the edges in both (a) and (b). (c) Exponential decay of the correction from the edges with varying magnetic field  $f$  and current  $I$ . The symbols correspond to the numerically calculated vertical phases. The solid lines come from our approximate solution  $\phi_j^V \ddagger$  and have slopes  $\pm \ln r$  given by (25).

To complete the solution, the constants  $P, Q$  in (24) have to be fixed from the boundary conditions

$$I = \sin(\pi f - B_1) + \sin(\arcsin I + A_1) \quad (26)$$

$$I + \sin(\pi f - B_N) = \sin(\arcsin I + A_{N+1}), \quad (27)$$

which result from current conservation at nodes 1 and  $N+1$  respectively. Since  $\{A_j, B_j\}$  become largest at the edges, equations (26)–(27) are solved numerically *without* linearization. When the array is long enough, such that  $\lambda \ll N+1$ , the effect of one edge on the other is negligible and the solution is further simplified as equations (26)–(27) decouple. Then  $Q$  and  $P$  are obtained independently by solving

$$I = \sin\left(\pi f + \frac{Q}{2} \left(1 - \frac{1}{r}\right)\right) + \sin(\arcsin I + Q) \quad (28)$$

$$I + \sin \left( \pi f - \frac{P}{2} \left( 1 - \frac{1}{r} \right) \right) = \sin(\arcsin I + P). \quad (29)$$

Figure 2 (a)–(b) shows that the above analytical solution agrees well with the results of simulations for long ( $N = 25$ ) arrays. The approximation accounts well for the effect of the open ends also for short ( $N = 7$ ) arrays (not shown). The exponential decay of the perturbation from the edges is also checked satisfactorily in Figure 2(c). As expected on physical grounds, the edge effects become more important as both the field and the current are increased. Thus, the approximation is best when  $f$  and  $I$  are small, and worsens as  $I \rightarrow 1$  and  $f \rightarrow 1/2$  ( $f = 1/2$  is a singular limit, as seen from the vanishing denominator in (22)). This establishes limits on the use of this approximation for the prediction of the depinning current at high values of the frustration.

Our analytical approximation also explains other features of the numerics. For instance, the corrections  $A_j, B_j$  are spatially asymmetric with respect to the center of the array when  $I > 0$  — as seen in Figure 2(a)–(b) by comparing the rightmost and leftmost phases. Note also that for  $0 < f \leq 1/2$  the largest vertical phase occurs at the right end of the ladder — in obvious connection with the preferred direction for flux-propagation in the array ( $-\hat{x}$ ). Moreover, it can readily be shown that the change of the frustration from  $f$  to  $1-f$  has only one effect: the vertical phases for frustration  $1-f$  are a mirror image, with respect to the center of the array, of the vertical phases with frustration  $f$ . This implies that the depinning current will be *identical* for both values of the frustration, as expected, but the direction of propagation is reversed<sup>20</sup>.

## B. Single-vortex solution

An analytical approximation for the single-vortex configuration can be obtained in a similar fashion by realizing that the effect of a vortex located in cell  $a$  of the array is similar to the edge effects in the no-vortex state. Note how, if the phases in Figure 3(a)–(b) were reduced to  $[-\pi, \pi]$ , the single-vortex configuration is composed of two halves, each of which is equivalent to a no-vortex superconducting solution when we move away from the edges and from the vortex center  $a$ .

Hence, the zeroth order single-vortex solution  $\{\phi_j^V, \phi_j^H\}$  is identical to the no-edge nv solution given in (17). And the edge and vortex-corrected approximation with a vortex distribution  $n_a = 1$  and  $n_j = 0, \forall j \neq a$  is given by

$$\phi_j^V = \arcsin I + A_j, \quad \phi_j^H = \pi f - B_j, \quad (30)$$

where the corrections  $\{A_j, B_j\}$  result now both from the presence of the edges and of the vortex in plaquette  $a$ .

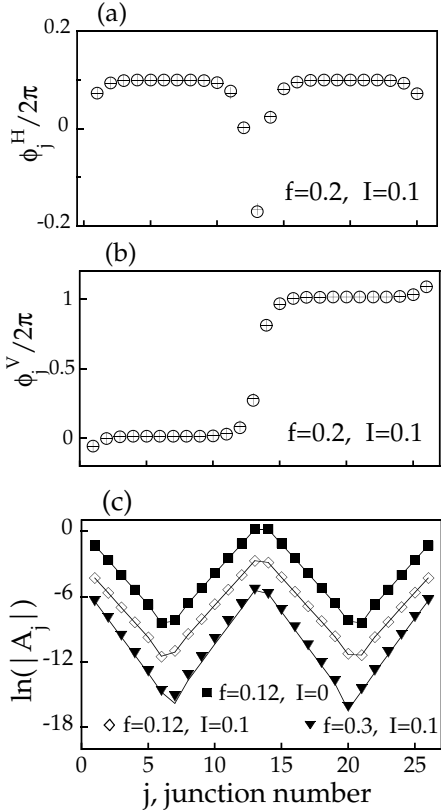


FIG. 3. Single-vortex solution. (a) Phases of the horizontal junctions for a  $25 \times 1$  ladder for  $I = 0.1$  and  $f = 0.2$  with a vortex in the central plaquette: numerical configuration from dynamical simulations (+), and analytical approximation (o) as given by (30). (b) Same as in (a) for the vertical junctions. The phases are not reduced to the  $[-\pi, \pi]$  interval. (c) Exponential decay of the correction  $A_j$  from both the edges and from the center of the vortex for different  $f$  and  $I$ . Symbols represent numerical simulations and the solid lines are the corresponding analytical predictions given by (31). The different graphs have been offset for clarity.

Following the same steps as for the nv configuration, we obtain identical expressions (19)–(25) for the corrections for *each* half of the array:

$$A_j = \begin{cases} Pr^{j-a} + Qr^{1-j}, & j \leq a \\ P'r^{j-(N+1)} + Q'r^{a+1-j}, & j > a \end{cases} \quad (31)$$

$$B_j = \frac{A_{j+1} - A_j}{2}, \quad j \neq a \quad (32)$$

where  $r$  is, once more, given by (25). Therefore, the single-vortex solution is obtained by *matching* two edge-corrected no-vortex solutions. In fact, the vortex in cell  $a$  effectively introduces two new “edges”, at  $a$  and  $a+1$ , which also produce similar exponentially decaying corrections. The matching condition at  $a$  and  $a+1$  is given by the fluxoid quantization condition in the cell containing the topological vortex:  $A_a - A_{a+1} + 2B_a = 2\pi$ . Thus,

$$B_a = \pi + \frac{P'r^{a-N} + Q' - P - Qr^{1-a}}{2}. \quad (33)$$

This completes the equations needed to determine the unknowns  $P, Q, P', Q'$  in our solution (31). They can be calculated numerically<sup>20</sup>, for given  $I$  and  $f$ , from (33) and the boundary conditions from current conservation at nodes 1,  $a$ ,  $a + 1$  and  $N + 1$ . The approximation is compared with numerical simulations in Figure 3 with excellent agreement, especially at small  $f$ .

We also note that although the ladder equations (15)–(16) can be reduced approximately to a discrete sine-Gordon equation<sup>13,14,19</sup>, our analytical expression (30) is a better approximation than the much-used sine-Gordon kink, which is a good description in strictly 1-D parallel arrays<sup>23</sup>. A detailed comparison of both approaches is presented in Appendix A.

### C. Fully-frustrated solution

The other relevant superconducting state is the fully-frustrated solution, which appears in simulations when  $f \approx 1/2$  (Figure 4). To obtain an analytical approximation, we follow once more the same scheme as above: first, calculate a no-edge basic solution; then, introduce the edges perturbatively.

In this case, the basic solution is seen numerically to oscillate in space with a wavelength equal to two plaquettes. Thus, when edges are neglected (the infinite-ladder approximation), the phases can be approximated in general by

$$\begin{cases} \phi_j^{V^\dagger} = 2\pi [a + (-1)^j b] \\ \phi_j^H = 2\pi [c + (-1)^j d] \end{cases} \quad (34)$$

where  $a, b, c, d$  are to be determined from (15)–(16) with  $n_j = [1 \mp (-1)^j]/2$ . First, substitution in Eq. (16) gives  $c$  and  $d$

$$c = f/2 - 1/4 \quad (35)$$

$$d = b \pm 1/4. \quad (36)$$

Second, from Eq. (16) we obtain

$$\begin{aligned} \sin 2\pi a \cos 2\pi b &= I \\ \sin 2\pi b \cos 2\pi a - 2 \sin \pi f \cos 2\pi b &= 0, \end{aligned}$$

from which we then solve explicitly for  $a$  and  $b$  in terms of the parameters  $f$  and  $I$

$$a = \frac{1}{2\pi} \arcsin \sqrt{L/2} \quad (37)$$

$$b = \frac{1}{2\pi} \arccos \sqrt{2I^2/L} \quad (38)$$

where

$$L = (1 + I^2) \pm \sqrt{(1 - I^2)^2 - 16I^2 \sin^2 \pi f}. \quad (39)$$

Figure 4 (a)–(b) compares the analytical infinite-ladder fully-frustrated approximation (34)–(39) with numerical simulations. The agreement is good except near the ends, as expected.

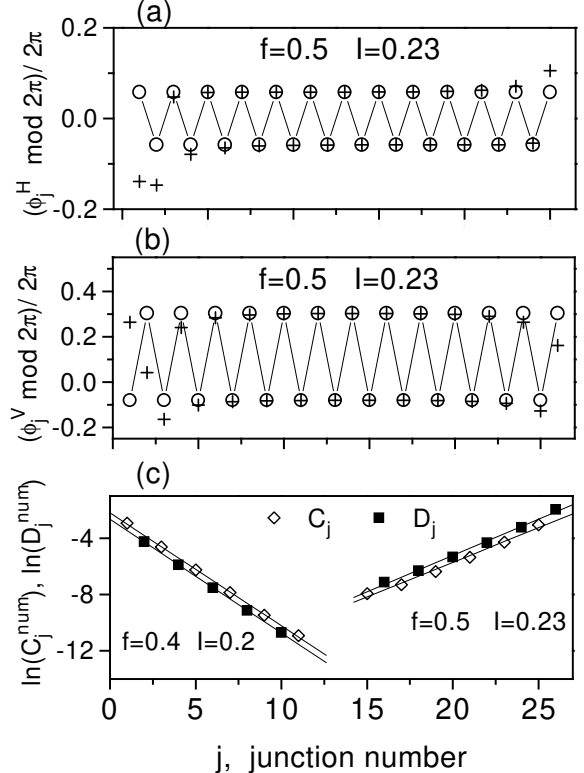


FIG. 4. Fully-frustrated solution. (a) Phases of the horizontal junctions for a  $25 \times 1$  with  $I = 0.23$  and  $f = 0.5$ . The numerical solution (+) and infinite-ladder analytical approximation  $\phi_j^{V^\dagger}$  (—o—) are seen to coincide except close to the edges. The solid line (a guide to the eye) emphasizes the wavelength equal to two plaquettes. (b) Same as (a) for the vertical junctions. (c) Exponential decay of the corrections from the edges in the fully-frustrated solution for varying  $f$  and  $I$ . Both the odd ( $C_i^{\text{num}}$ ) and even ( $D_i^{\text{num}}$ ) site corrections have a characteristic length  $\pm (\ln r)/2$  given by (49). The solid lines are best linear fits with slopes  $-0.805$  (for  $f = 0.4, I = 0.2$ ) and  $0.502$  (for  $f = 0.5, I = 0.23$ ). They are in excellent agreement with the predicted values  $(\ln r)/2$  from (49), which are  $0.806$  and  $0.488$ , respectively.

The approximation above also yields an existence criterion for the no-edge fully-frustrated solution. In (39), the expression inside the square root must be non-negative; hence the infinite-ladder fully-frustrated solution does not exist if

$$I > I_{\text{ff,th}} = \sqrt{4 \sin^2 \pi f + 1 - 2 \sin \pi f}, \quad (40)$$

where the subscript “ff” denotes fully-frustrated and “th” denotes a theoretical approximation of a bifurcation con-

dition. We will use this condition (40) later when we discuss the depinning of the fully-frustrated solution.

This predicted form of the infinite-ladder fully-frustrated solution agrees with previous findings obtained for the special case when there is no driving current<sup>15</sup>. For  $I = 0$ , our solution (34)–(39) reduces to the stable configuration<sup>24</sup>

$$\phi_j^{V\dagger} = (-1)^j \arctan(2), \quad \phi_j^{H\dagger} = (-1)^{j+1} \arctan(1/2),$$

which coincides with the ground state for  $f = 1/2$  and  $I = 0$  calculated by Benedict<sup>15</sup>. (To obtain this result from the expressions above, note that  $2I^2/L \rightarrow (1 + 4\sin^2 \pi f)^{-1}$  as  $I \rightarrow 0$ , for the solution corresponding to the minus sign in (39).) We also note that the infinite-ladder fully-frustrated solution exists for all  $f$  when  $I = 0$ , i.e., there is no critical magnetic field below which it ceases to exist, although it is energetically most favorable when  $f \approx 1/2$ .

The physical meaning of this solution is clear: it contains a topological vortex in every other cell, as seen from the alternating sequence of zeros and ones for the plaque integers  $\{n_j\}$  in the equations (15)–(16).

In fact, although the solutions with  $\{n_{\text{odd}} = 1, n_{\text{even}} = 0\}$  and  $\{n_{\text{odd}} = 0, n_{\text{even}} = 1\}$  are degenerate in an infinite array, they are not so if the array is finite. However, we will show in Section V that the depinning of the fully-frustrated state is basically unaffected by the parity of the number of cells in the ladder.

As we did for the no-vortex solution, we now introduce corrections from the edges. The improved solution  $\{\phi_j^{V\dagger}, \phi_j^{H\dagger}\}$  is given by

$$\begin{cases} \phi_{2i-1}^{V\dagger} = \phi_{\text{odd}}^{V\dagger} + C_i \\ \phi_{2i}^{V\dagger} = \phi_{\text{even}}^{V\dagger} + D_i \end{cases}, \begin{cases} \phi_{2i-1}^{H\dagger} = \phi_{\text{odd}}^{H\dagger} - E_i \\ \phi_{2i}^{H\dagger} = \phi_{\text{even}}^{H\dagger} - F_i \end{cases} \quad (41)$$

where  $i = 1, \dots, \text{ceil}(N/2)$  and there is an additional  $\phi_{N+1}^{V\dagger}$  when  $N$  is even and  $\phi_{N+1}^{H\dagger} = 0$  when  $N$  is odd. The double cell is used to simplify the calculations, as suggested by the spatial periodicity of the infinite-ladder solution.

Again, far away from the ends the corrections are small and we linearize the governing equations (15)–(16) around the basic solution (34). Thus we obtain the following system of coupled difference equations:

$$C_i - D_i + 2E_i = 0 \quad (42)$$

$$D_i - C_{i+1} + 2F_i = 0 \quad (43)$$

$$-E_i \cos \phi_{\text{odd}}^{H\dagger} = -F_i \cos \phi_{\text{even}}^{H\dagger} + D_i \cos \phi_{\text{even}}^{V\dagger} \quad (44)$$

$$-F_i \cos \phi_{\text{even}}^{H\dagger} = -E_{i+1} \cos \phi_{\text{odd}}^{H\dagger} + C_{i+1} \cos \phi_{\text{odd}}^{V\dagger}. \quad (45)$$

Eliminating  $E_i, F_i$  and  $D_i$  we get a second-order difference equation for  $C_i$ :

$$C_{i+2} + 2\gamma C_{i+1} + C_i = 0, \quad (46)$$

with  $\gamma(I, f)$  given by

$$\gamma = \frac{\sin^2 \pi f + cb^2 \cos 2\pi f - 2[(\sin^2 \pi f - sa^2)sb^2 + ca^2]}{\sin^2 \pi f - cb^2}. \quad (47)$$

(Here  $sa, sb, ca$  and  $cb$  are shorthand for  $\sin 2\pi a, \sin 2\pi b, \cos 2\pi a$  and  $\cos 2\pi b$  respectively). This difference equation has the general solution

$$C_i = Pr_{\text{ff}}^i + Qr_{\text{ff}}^{-i} \quad (48)$$

$$\text{with } r_{\text{ff}} = -\gamma + \sqrt{\gamma^2 - 1} \equiv e^{1/\lambda_{\text{ff}}}. \quad (49)$$

And  $r_{\text{ff}}$  is related again to another characteristic penetration depth for the perturbations from the edges to die off, this time inside a region with the fully-frustrated solution. The coefficients  $P$  and  $Q$  have to be calculated numerically using the boundary conditions from nodes 1 and  $N + 1$ . The spatial dependence of  $D_i$  is also of the same form  $D_i = Rr_{\text{ff}}^i + Sr_{\text{ff}}^{-i}$ . Note that in both equations,  $i$  is the number that indexes the double cell.

Figure 4 (c) illustrates the accuracy of these approximate formulas. Specifically, we plot the spatial dependence of the predicted deviations

$$C_i^{\text{num}} = \phi_{2i-1}^V - \phi_{2i-1}^{V\dagger}, \quad D_i^{\text{num}} = \phi_{2i}^V - \phi_{2i}^{V\dagger},$$

where  $\phi_j^V$  is obtained from the numerical solution and  $\phi_j^{V\dagger}$  is the infinite-ladder approximation. The expected exponential decay close to the edges with characteristic length  $\lambda_{\text{ff}} = 2/\ln r_{\text{ff}}$  is verified in the figure.

#### IV. DYNAMICAL DEPINNING TRANSITIONS OF THE ARRAY

In this section, we describe the depinning transitions as seen in dynamical simulations of the ladder array at zero temperature. In the following section, we will explain these dynamical results by relating them to the bifurcations of the no-vortex, single-vortex, and fully-frustrated superconducting solutions. The main goal is to give a rigorous mathematical explanation of the following observations: Dynamical simulations show that the array is superconducting at low values of the driving current  $I$ . As  $I$  is increased, the array remains superconducting until a critical current  $I_{\text{dep}}(f)$  is reached, after which the array depins and develops a non-zero average voltage. This depinning current  $I_{\text{dep}}$  decreases monotonically as the frustration  $f$  increases from 0 to 1/2.

These numerical observations are all at the averaged level of the  $IV$  characteristics. They do not tell us anything about the detailed configuration of the individual junctions. In particular, there are several distinct superconducting states (e.g., the nv, sv, and ff states discussed in Section III, and states containing multiple vortices) but these are indistinguishable on the  $IV$  curve. This ambiguity raises the question: what is the state of the ladder just before it depins?

We will show in Section V that for most values of  $f$ , the depinning of the ladder is caused by the destruction of the no-vortex state. Specifically, the global depinning current  $I_{\text{dep}}(f)$  can be predicted by calculating the current at which the no-vortex state is annihilated in a saddle-node bifurcation. The only exception occurs for values of  $f$  close to  $1/2$ , where the depinning is due to saddle-node bifurcations of states of the fully-frustrated type. The noteworthy point here is that no other superconducting states play a role in the global depinning of the array.

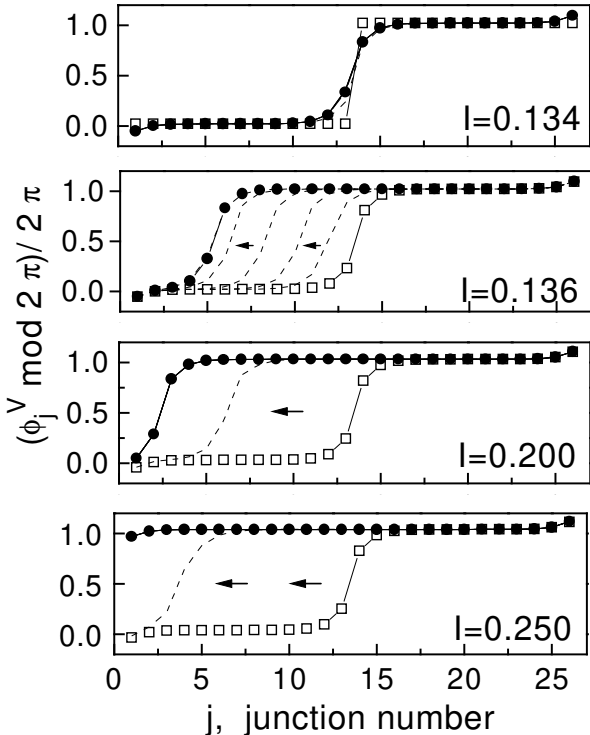


FIG. 5. Snapshots of the time-evolution of the single-vortex solution for a  $25 \times 1$  ladder array with  $\beta_c = 10$  and  $f = 0.2$  and increasing  $I$ . Initial (□), intermediate (—), and final (●) configurations are shown. At  $I = 0.134 < I_{\text{LAT}}$  the initial configuration with a  $2\pi$ -jump relaxes to the stationary single-vortex solution. When  $I = 0.136 \simeq I_{\text{LAT}}$  the vortex becomes dislodged from the center. It moves slowly to the left and then stops at some intermediate position between the center and the edge. For  $I_{\text{LAT}} < I = 0.2 < I_{\text{left}}$  the vortex moves until it gets pinned near the edge, where the potential barrier is larger. Finally, at  $I_{\text{left}} < I = 0.25 < I_{\text{dep}}$  the vortex is expelled from the array and the *no-vortex solution* is recovered.

However, the question arises as to how the depinning behavior would change when configurations with vortices are used as initial conditions (rather than the random or zero-phase initial conditions that we ordinarily use in our

simulations of the *IV* characteristics). To address this issue, we perform dynamical simulations from an initial condition with one  $2\pi$ -step in the middle cell of the array:

$$\phi_j^H(t=0) = 0, \quad \phi_j^V(t=0) = 2\pi \Theta \left( j - \text{ceil} \left( \frac{N+1}{2} \right) \right),$$

where  $\Theta(x)$  is the Heaviside step function. This initial condition is *not* a solution of the system and, thus, under the dynamical equations (12)–(14) it relaxes onto a true solution for the ladder. For most  $\{f, I\}$ , the *single-vortex superconducting state* (top panel of Figure 5) is reached, i.e., a static configuration with a topological vortex in cell  $a$  of the array such that  $n_a = 1$  and  $n_j = 0$ ,  $\forall j \neq a$ ,  $j = 1, \dots, N$ . For some ranges of  $f$  and  $I$ , this configuration is not dynamically stable and other solutions are found, as discussed in Section V.

The numerical observations shown in Figure 5 depict the dynamical behavior of the single-vortex state for most values of  $f$ , i.e. approximately  $0.12 < f < 0.37$ . They can be summarized as follows: For  $f > f_{\text{min}}$  and small driving current  $I$ , the system relaxes onto a static single-vortex solution with a vortex in the middle of the array. The solution is slightly distorted as the current is increased, until at  $I = I_{\text{LAT}}(f)$  the vortex moves from the center cell toward the left. (This current is analogous to the well-known Lobb-Abraham-Tinkham (LAT) depinning current for two-dimensional Josephson junction arrays<sup>25</sup>). For currents very close to  $I_{\text{LAT}}$ , the vortex moves slowly and gets trapped in another cell somewhere between the center and the edge. For somewhat larger  $I > I_{\text{LAT}}$ , the vortex moves all the way to the left edge where it becomes pinned until, at a second critical current  $I_{\text{left}}$ , it is expelled from the array and the no-vortex solution is recovered again. The no-vortex configuration then remains stable until, at  $I_{\text{dep}}$ , global depinning of the array occurs. If instead of placing the vortex in the middle, we locate it closest to the *right* edge, it depins at a current  $I_{\text{right}} < I_{\text{LAT}}$ , and moves toward the center.

These observations can be clarified with the usual analogy<sup>26</sup> of the vortex as a damped particle moving in a sinusoidal potential under the action of a  $-\hat{x}$  Lorentz-like force directly proportional to  $I$ . The maxima of the potential correspond to the vertical junctions and the minima are situated in the middle of the cells. Thus, the initial barrier which has to be overcome to begin the motion explains the critical  $I_{\text{LAT}}$ . Moreover, the open boundaries can be thought to produce an exponentially-decaying envelope superimposed on the sinusoidal potential. Thus the motion of the vortex is easier when the vortex is close to the right edge and becomes increasingly difficult as the left boundary is approached. When  $I_{\text{left}}$  is reached, the vortex is able to overcome the edge barrier and is expelled from the array. Then the no-vortex configuration is recovered and no new vortex enters the ladder.

We mentioned before that the described behavior is observed for values of the frustration contained between

two limiting values. First, there is a minimum frustration  $f_{\min} \sim 0.12$  below which the single-vortex solution never ensues from this initial condition; in fact, the system settles on the no-vortex superconducting solution. Second, for  $f$  larger than  $\sim 0.37$ , the vortex is *not* expelled from the array at the left edge before depinning. Depinning occurs in that case when vortices enter the array from the right edge. These observations will be clarified in Section V.

We have also performed dynamical simulations for the multi-vortex case and reached similar conclusions for most values of  $f$ . In that case, the initial condition consists of  $Nf$  equally spaced  $2\pi$ -steps which are then allowed to evolve dynamically. For  $I = 0$  and large enough  $f$ , the initial condition relaxes onto the expected solution with  $Nf$  vortices in the array. As the current is increased, these move towards the left end where they accumulate until they are expelled one by one at different currents. After this, the no-vortex solution is again recovered.

On the other hand, the picture changes when  $f$  is close to  $1/2$ . There, solutions of the fully-frustrated type are obtained from the multi-vortex initial condition and there is no expulsion of vortices from the ladder. Instead, the array depins globally at the current where the ff solution ceases to exist, i.e.  $I_{\text{dep}}(f \rightarrow 1/2) \approx I_{\text{ff,th}}$ .

We conclude that in the ladder, the depinning of one vortex (or a train of vortices) is *not* equivalent to the global edge-dominated depinning of the device. As we will confirm in Section V, the no-vortex and fully-frustrated states are the relevant solutions for the depinning of the array; for moderate  $f$ , even if the initial conditions contain vortices, these are expelled from the array as the current is increased and, eventually, the no-vortex solution is recovered. For  $f$  close to  $1/2$ , the system settles onto fully-frustrated solutions with distinct depinning properties.

We have also identified three other critical currents related to the single-vortex configuration:  $I_{\text{right}}$ , at which a vortex at the right edge begins to move;  $I_{\text{LAT}}$ , at which dynamical depinning occurs for a single vortex centered in the middle of the ladder; and  $I_{\text{left}}$ , at which the vortex is expelled at the edge.

All of these dynamical observations are explained in detail in the next section where they are compared to their exact mathematical descriptions.

## V. BIFURCATION ANALYSIS OF THE DEPINNING TRANSITIONS

In this section, we use bifurcation theory to obtain exact criteria for all the critical currents of the no-vortex, single-vortex, and fully-frustrated states. We have checked consistently that these bifurcations explain the dynamical depinning behavior of the array as described in Section IV. Furthermore, analytical simplifications to some of those criteria will be deduced from approximations of the exact depinning results.

The depinning of the ladder can be explained in dynamical terms as follows: The linear stability of the superconducting states of the ladder as a function of  $I$  can be deduced from the Jacobian matrix  $\mathbf{J}_{\text{dyn}}$  of the dynamical system (12)–(14) for a given value of  $f$ , and for a given fixed point—in particular, the no-vortex, single-vortex or fully-frustrated state. If all the eigenvalues have negative real parts, the fixed point is linearly stable. As we increase  $I$ , some of the eigenvalues move to the right in the complex plane, and the fixed point becomes less stable. The critical current for a given fixed point is defined by the condition that the maximum of the real parts of the eigenvalues becomes positive. Then, to predict the *global* depinning current, we compare the critical currents of the different superconducting states, and take the maximum of those. In other words, we predict that global depinning occurs when the “last” stable state bifurcates.

Recall that there are several scenarios<sup>10</sup> by which a stable fixed point can undergo such a bifurcation. First, in a zero-eigenvalue bifurcation, a single eigenvalue moves along the real axis, and passes from negative to positive at the bifurcation. There are three main subtypes of zero-eigenvalue bifurcation: saddle-node, transcritical, and pitchfork. In the saddle-node bifurcation, a stable fixed point collides with a saddle point, and both are annihilated. In contrast, in the transcritical and pitchfork bifurcations, the stable fixed point is not destroyed—it continues to exist but goes unstable. A second scenario is provided by the Hopf bifurcation which involves a pair of complex conjugate eigenvalues passing through the imaginary axis from the left half plane to the right half plane—again this bifurcation destabilizes the fixed point, but does not destroy it.

Since it can be shown that Hopf bifurcations are not possible in this system<sup>27</sup>, we can simplify our calculations by using the *static* system (15)–(16) to identify the location of the zero-eigenvalue bifurcations. Those bifurcation points are characterized by a change in the number of fixed points and, thus, from the implicit function theorem<sup>28</sup>, the Jacobian matrix  $\mathbf{J}$  of the static system has zero determinant there. Hence, we use the superconducting (static) up-down symmetric system given by  $\mathbf{f}(\mathbf{x}) = \mathbf{0}$ ,

$$f_i(\mathbf{x}) = I + \sin x_{N+i} - \sin x_{N+1+i} - \sin x_i, \quad i = 1, \dots, N+1 \quad (50)$$

$$f_{N+1+i}(\mathbf{x}) = x_i - x_{i+1} - 2x_{N+1+i} + 2\pi(f - n_i), \quad i = 1, \dots, N \quad (51)$$

with  $\mathbf{x} = (x_1, \dots, x_{2N+1}) \equiv (\phi_1^V, \dots, \phi_{N+1}^V, \phi_1^H, \dots, \phi_N^H)$ . For a given  $f$  and a given superconducting state, we compute the bifurcating fixed point  $\mathbf{x}^*$  and its associated critical current  $I^*(f)$  at which  $\det(\mathbf{J}) = 0$ . To this end, we define an augmented algebraic system with the current  $I$  as an extra variable, and the constraint on the determinant as an extra equation. Then  $\mathbf{x}^*$  and  $I^*$  are obtained by solving  $\mathbf{F}(\mathbf{X}^*) = \mathbf{0}$  where  $\mathbf{X} = (\mathbf{x}, I)$  and

$$F_j(\mathbf{X}) = f_j, \quad j = 1, \dots, 2N + 1 \quad (52)$$

$$F_{2N+2}(\mathbf{X}) = \det(\mathbf{J}). \quad (53)$$

Figure 6 shows that the dynamical depinning of the ladder is explained by  $I^*$  (zero-eigenvalue) bifurcations.

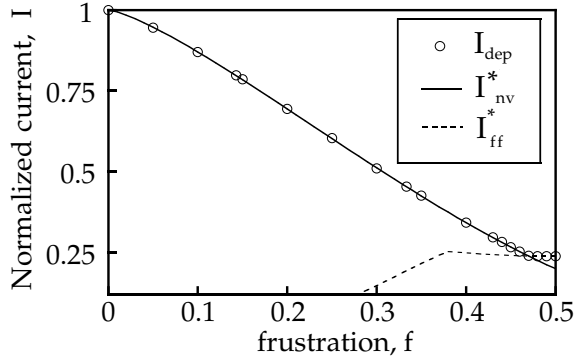


FIG. 6.  $f$ -dependence of the global depinning current of the array. The numerical  $I_{\text{dep}}(\circ)$  is obtained by sweeping the current up from zero in dynamical simulations; no assumptions are made about the state of the system. The static current  $I_{\text{nv}}^*$  marks the point where a particular superconducting state, the no-vortex solution, is destroyed in a saddle-node bifurcation. Similarly,  $I_{\text{ff}}^*$  corresponds to the maximum of the saddle-node bifurcation currents for solutions of the fully-frustrated type.

The rest of this section is devoted to analyzing the bifurcations of the no-vortex, single-vortex and fully-frustrated configurations. For the sake of clarity, we follow a parallel scheme for all of them and keep the notation consistent. For each of the states, we first calculate numerically the zero-eigenvalue bifurcations from (52)–(53) (always denoted with a star  $*$ ) and compare them with the depinning currents from *dynamical* simulations (always denoted with symbols in the figures). Then, when possible, we deduce analytical simplifications of these criteria in one of two ways: (a) by deducing that the instability is essentially caused by a bifurcation of the no-edge solution, or (b) by explaining the instability as edge-originated and, thus, localized at the boundaries. These theoretical analytical approximations are always denoted with the subscript “th”. Moreover, to emphasize the importance of the edges in the depinning transitions, we calculate the depinning of the no-edge solutions for all three configurations. Finally, note that no energy arguments are invoked in this discussion. Thermodynamic considerations are studied in detail in Section VI where phase diagrams of these superconducting states for the no-edge and finite ladders are presented.

## A. Bifurcation of the no-vortex solution

Figure 6 shows that for most values of  $f$ , the depinning current  $I_{\text{dep}}(f)$  (obtained from dynamical simulations) coincides with the critical current  $I_{\text{nv}}^*$  for the no-vortex state—calculated from the augmented system (52)–(53). Indeed, we find that the bifurcating phase configuration  $\mathbf{x}_{\text{nv}}^*$  matches the depinning configuration  $\mathbf{x}_{\text{dep}}$  observed in dynamical simulations. Hence, the bifurcation of the no-vortex state constitutes an exact criterion for the global depinning current, except for values of  $f$  close to  $1/2$ , where the global depinning is caused by the destruction of the fully-frustrated solution, as explained below.

To gain intuition about how to derive analytical approximations for  $I_{\text{dep}}(f)$ , it is helpful to characterize the depinning bifurcation more precisely. Our numerical computations indicate that the depinning of the no-vortex state is due to a saddle-node bifurcation. As  $I$  approaches  $I_{\text{nv}}^*$  from below, the stable no-vortex state approaches an unstable no-vortex state, and coalesces with it when  $I = I_{\text{nv}}^*$ , causing both states to disappear. Figure 7(a) shows the maximum *dynamical* eigenvalue for both the stable and unstable states—note that both of these eigenvalues are pure real, and they equal 0 at the critical current. As expected, this plot has the standard shape of a saddle-node bifurcation diagram<sup>10</sup>. Figure 7(b)–(c) plots the phase configuration for both states at  $I = 0$ . They have similar spatial structure, except near the rightmost cell, where (in the language of the mechanical analog) the unstable state has an inverted pendulum.

Incidentally, Figure 7 also shows that both states satisfy the up-down symmetry  $\phi_j^H = -\phi_j^h$  discussed in Section II. Numerical simulations show that this symmetry continues to hold for all values of  $I$  on both the stable and unstable branches. Thus, the global depinning bifurcation takes place entirely within the invariant manifold of up-down symmetric states—it is *not* a symmetry-breaking bifurcation.

### 1. Analytical approximations for $I_{\text{nv}}^*(f)$

The conclusion that the depinning transition for most values of  $f$  corresponds to a saddle-node bifurcation of the no-vortex superconducting state can be simplified further. We now obtain analytical approximations for  $I_{\text{nv}}^*(f)$  using the approximate solutions calculated in Section III.

We recall that the bifurcation of the infinite-ladder no-vortex configuration does not explain the observed  $f$ -dependence of the finite-ladder nv depinning. As discussed in Section III, if the edges are neglected completely, the no-vortex solution (18)–(24) is predicted to exist and be stable for all  $I < 1$ , independent of the frustration  $f$ , in analogy with the single junction. Thus,

the depinning for the no-edge nv state occurs through a saddle-node bifurcation at  $I_{\text{nv,th}}^\dagger(f) = 1$ ,  $\forall f$ .

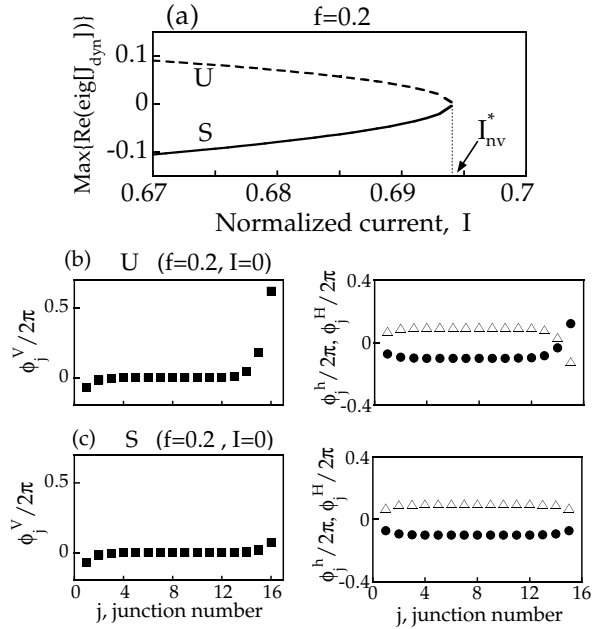


FIG. 7. Saddle-node bifurcation of the no-vortex solution in a  $15 \times 1$  ladder. (a) Value of the maximum of the real parts of the eigenvalues of the dynamic Jacobian matrix  $\mathbf{J}_{\text{dyn}}$  for the stable (S, solid line) and unstable (U, dashed line) branches with  $f = 0.2$  and  $\beta_c = 0.25$ . They collide and annihilate at  $I_{\text{nv}}^*$  in a saddle-node bifurcation. We remark that, although the eigenvalues change with  $\beta_c$ , the bifurcation point  $I_{\text{nv}}^*$  is independent of  $\beta_c$ . (b) Phase configuration of the vertical (left) and horizontal (right) junctions for the unstable branch (U) at  $f = 0.2$  and  $I = 0$ . (c) Same as (b) for the stable branch (S). Note that both configurations (b)–(c) are up-down symmetric, and the unstable branch (b) corresponds to an inverted pendulum at the rightmost cell.

To capture the observed  $f$ -dependence of the critical current  $I_{\text{nv}}^*$ , we need a more careful approximation. We now present two such approximations to  $I_{\text{nv}}^*$  that clarify the physical picture of the transition.

The first strategy is to use the improved approximation (18) for the no-vortex state (in which the edge effects are included perturbatively), and then write down a *simplified augmented system*  $\mathbf{F}^\ddagger(\mathbf{X}^\ddagger) = \mathbf{0}$  for this solution, similar to the expression (52)–(53) for the full  $(2N+2)$ -dimensional system. We can then calculate the critical current  $I_{\text{nv,red}}$  for this reduced model, defined as the value of  $I$  where the *perturbative* solution under-

goes a saddle-node bifurcation. This renders the calculation analytically tractable since, for a given  $f$ , only three variables  $\{P, Q, I\}$  suffice to describe the perturbative solution (18)—instead of  $I$  and  $2N+1$  phases for the full solution. The simplified augmented system is constituted by (28), (29) together with the condition that the determinant of the  $2 \times 2$  Jacobian matrix equals zero, corresponding to the zero-eigenvalue condition at a saddle-node bifurcation.

Furthermore, since equations (28) and (29) are uncoupled when  $N$  is not very small, even this three-dimensional system can be further reduced to a two-dimensional system with unknowns  $P$  and  $I$ :

$$\mathbf{F}_1^\ddagger = I + \sin\left(\pi f - \frac{P}{2}\left(1 - \frac{1}{r}\right)\right) - \sin(\arcsin I + P) \quad (54)$$

$$\mathbf{F}_2^\ddagger = \frac{\partial \mathbf{F}_1^\ddagger}{\partial P} \quad (55)$$

where  $r = r(f, I)$  is given by (25). Note that this is a set of *local* equations referred to the rightmost end of the array. We numerically solve the  $2 \times 2$  reduced system  $\mathbf{F}^\ddagger(P_{\text{red}}, I_{\text{nv,red}}) = \mathbf{0}$  to obtain the approximate depinning current  $I_{\text{nv,red}}(f)$  and the value of the rightmost phase  $P_{\text{red}}$  at the bifurcation.

Figure 8 shows that  $I_{\text{nv,red}}(f)$  predicts the exact  $I_{\text{nv}}^*(f)$  reasonably well. As expected, the prediction gets worse as  $f$  nears  $1/2$  since the perturbative approximation of the no-vortex solution is less accurate in that limit.

Both the analyses of the eigenfunctions of the full  $2N+2$  system (52)–(53) and of the reduced system (54)–(55) indicate that the global depinning of the ladder is caused by a local instability of the rightmost junction of the array. This is consistent with physical arguments which imply that after depinning occurs, vortices propagate in the array in the  $-\hat{\mathbf{x}}$  direction under the effect of a magnetic Magnus (Lorentz-like) force.

The key role played by the rightmost junction suggests a second simplification, which we call a heuristic criterion for depinning. This criterion connects the global depinning of the ladder with the much simpler depinning transition in a single junction. Recall that when the phase of a single junction reaches  $\pi/2$ , its superconducting solution is destroyed in a saddle-node bifurcation<sup>10</sup>. Therefore, we intuitively propose that when the phase of the rightmost junction reaches  $\pi/2$ , the ladder depins. Replacing the no-vortex solution by its perturbative approximation (18), we solve for the current  $I_{\text{nv,th}}$  by imposing

$$\phi_{N+1}^V = \pi/2 \quad (56)$$

which implies

$$\arcsin I_{\text{nv,th}} + P(I_{\text{nv,th}}) = \pi/2. \quad (57)$$

Then, from (29), we obtain an implicit transcendental equation for  $I_{\text{nv,th}}(f)$ :

$$\arcsin(1 - I_{\text{nv,th}}) + \frac{r-1}{2r} \arccos I_{\text{nv,th}} = \pi f \quad (58)$$

with  $r = r(I_{\text{nv,th}})$  given by (25). This simple analytical prediction is shown to be in very good agreement with the exact results in Figure 8.

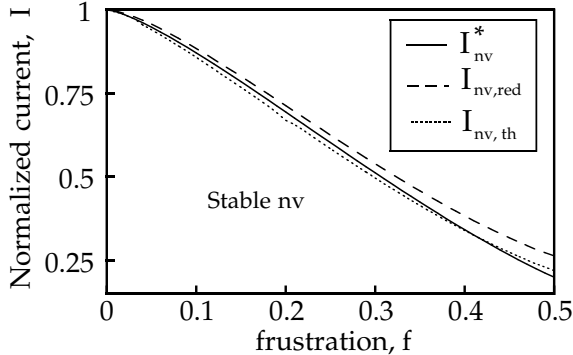


FIG. 8. Analytical simplifications  $I_{\text{nv,red}}$  and  $I_{\text{nv,th}}$  provide approximations to the critical current for the no-vortex solution  $I_{\text{nv}}^*$  by concentrating on the rightmost cell of the array.

The techniques described in this Section can be extended to include the effect of self-fields. In Appendix B we illustrate this approach and show how self-inductance modifies the approximate no-vortex solution and the corresponding depinning current.

### B. Bifurcations of the single-vortex solution

We begin the study of the stability of the single-vortex (sv) configuration by considering the single-vortex far from the edges. The results obtained for the vortex in the center will be used subsequently to describe the effects of the edges on the sv state.

#### 1. Saddle-node bifurcation of the sv solution

As described in Section IV, a vortex in the center of the array moves to the left over the potential barrier when the critical current  $I_{\text{LAT}}$  is reached. We show now that this depinning of the vortex corresponds to a saddle-node bifurcation of the single-vortex solution. To verify this, we restrict our attention to the single-vortex solutions that are centered in the middle of the ladder; then we look for the current  $I_{\text{sv}}^*$  at which the determinant of the static Jacobian matrix  $\det(\mathbf{J}|_{\mathbf{x}_{\text{sv}}^*}) = 0$ . As in (52)–(53), we solve the augmented system  $\mathbf{F}(\mathbf{x}_{\text{sv}}^*, I_{\text{sv}}^*) = \mathbf{0}$  to find where the centered single-vortex state ceases to exist.

Figure 9 shows the perfect agreement between the  $I_{\text{sv}}^*(f)$  computed from the static augmented system and the  $I_{\text{LAT}}(f)$  obtained from simulations where a vortex is placed in the middle of the array and the current is increased until it moves, i.e.,  $I_{\text{LAT}} = I_{\text{sv}}^*$ .

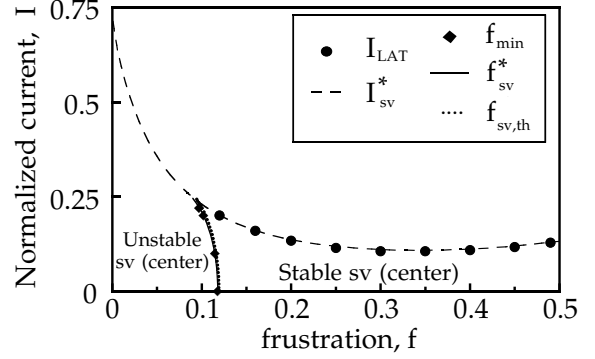


FIG. 9. Stability diagram for the single vortex in the center of the array.  $I_{\text{LAT}}(\bullet)$  is calculated dynamically from numerical simulations by sweeping the current until a vortex placed in the center of a  $25 \times 1$  array moves. These dynamical results ( $\bullet$ ) are well predicted by the static  $I_{\text{sv}}^*$  at which the fixed point corresponding to the pinned vortex ceases to exist (dashed line). Another dynamic instability of the single-vortex configuration at  $f_{\text{min}}$  (solid diamonds) is identified as a symmetry-breaking subcritical pitchfork bifurcation  $f_{\text{sv}}^*$ . It can be approximated with an analytical criterion  $f_{\text{sv,th}}$  given by (59). This approximation is so accurate that the curves for  $f_{\text{sv}}^*$  and  $f_{\text{sv,th}}$  are practically indistinguishable.

Moreover, Figure 10 confirms that this depinning transition is indeed caused by a saddle-node bifurcation. An unstable single-vortex state collides with and annihilates the stable single-vortex state at the transition. Figure 10 shows that the two states have similar spatial structure—the difference is that the stable state has its vortex in the center of a cell (where the vortex sits in a potential well), while the unstable state has its vortex on a junction (poised on a potential hill).

Although conceptually similar, our  $I_{\text{LAT}}$  for the ladder is not equivalent to that calculated by Lobb-Abraham-Tinkham<sup>25</sup>. Their current is estimated by a static calculation of the energy barrier  $E_b$  in an infinitely extended two-dimensional array, while ours is the dynamic current at which the centered single-vortex state undergoes a saddle-node bifurcation in the quasi-one-dimensional ladder. Moreover, their static calculation does not include the effects of the field  $f$  or the injected current  $I$  on the solutions while, in our case, they are implicitly taken into account since the configurations—and therefore their stability—depend parametrically on  $\{I, f\}$ .

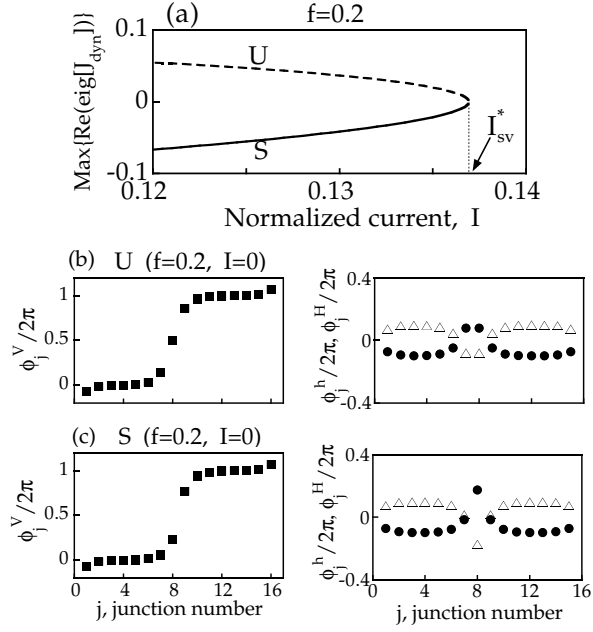


FIG. 10. Saddle-node bifurcation of the single-vortex solution at the center of a  $15 \times 1$  ladder. (a) Value of the maximum of the real parts of the eigenvalues of  $\mathbf{J}_{\text{dyn}}$  for the stable (S, solid line) and unstable (U, dashed line) branches with  $f = 0.2$  and  $\beta_c = 0.25$ .  $I_{\text{sv}}^*$  is the point where a saddle-node bifurcation occurs for this particular configuration. As in Fig. 7, the bifurcation point is independent of  $\beta_c$ . (b) Phases of the vertical (left) and horizontal (right) junctions for the unstable branch (U) at  $f = 0.2$  and  $I = 0$ . (c) Same as (b) for the stable branch (S). Again, both configurations (b)–(c) are up-down symmetric. Note that the stable branch (c) is associated with a vortex located at the center of a plaquette (a minimum of the potential), whereas the unstable branch (b) corresponds to a vortex centered around a junction (a local maximum of the potential energy).

## 2. Symmetry-breaking bifurcation of the sv solution

We noted above the numerical observation<sup>18</sup> that, when performing dynamical simulations, the static single-vortex solution is unstable below a *critical field*  $f_{\min}(I)$ . We show now that this is the result of a symmetry-breaking instability which is mathematically related to another zero-eigenvalue bifurcation. Therefore, once again, the dynamical  $f_{\min}$  coincides with a static  $f_{\text{sv}}^*$  calculated from the augmented system (52)–(53) as the value of  $f$  where the determinant of the static Jacobian matrix  $\mathbf{J}$  is zero and, thus, a change in the number of

fixed points is likely. Excellent agreement between  $f_{\min}$  and  $f_{\text{sv}}^*$  is shown in Figure 9.

Figure 11 depicts detailed information about this bifurcation. Specifically, it shows three single-vortex states that co-exist for  $f$  slightly greater than  $f_{\text{sv}}^*$ . These states appear very similar, but on close inspection, one notices that two of the states are asymmetric:  $\phi_j^H \neq -\phi_j^h$  (this is especially clear for the central plaquette  $j = a$ ). As  $f \rightarrow f_{\text{sv}}^*$  from above, these asymmetric states – which are unstable – simultaneously collide with the stable symmetric state, rendering it unstable. To visualize this transition in greater detail, Figure 11 plots the asymmetry for the central plaquette,  $S \equiv \phi_a^H + \phi_a^h$ , as a function of the frustration  $f$ . The symmetric state exists both above and below the bifurcation, and satisfies  $S = 0$  throughout. The two unstable branches join the symmetric branch at  $f = f_{\text{sv}}^*$ . The scenario depicted in Figure 11, common in symmetric systems, is known as a subcritical pitchfork bifurcation<sup>10</sup>.

From this, we conclude that there exists a region of the  $(f, I)$  plane (Figure 9) where the single-vortex configuration exists but is always dynamically unstable. In this region, the vortex (magnetic flux) is expelled *transversally* from the array through transient modes which do *not* preserve the up-down symmetry of the horizontal phases.

We can also derive an analytical expression  $f_{\text{sv,th}}$  for the critical field  $f_{\text{sv}}^*$ . As given in (11), all up-down symmetric fixed points become unstable when the phase of any of the horizontal junctions is larger than  $\pi/2$  in absolute value. Since this largest phase occurs at the central plaquette (as seen in Figure 11), the following stability criterion ensues from the condition  $\phi_a^H = -\pi/2$ :

$$2\pi f_{\text{sv,th}} + [P(f_{\text{sv,th}}) - Q'(f_{\text{sv,th}})] = \pi, \quad (59)$$

where we have used (30) and (33) and we consider a long array such that the effect of the edges on the middle cell can be neglected. Here  $P, Q'$  have to be calculated from the boundary conditions (current conservation) at nodes  $a$  and  $a + 1$ :

$$\begin{aligned} I + \sin(\pi f - P(r - 1)/(2r)) &= \\ \sin(\arcsin I + P) - \sin(\pi f - (Q' - P)/2) &= \\ I - \sin(\pi f - (Q' - P)/2) &= \\ \sin(\arcsin I + Q') + \sin(\pi f + Q'(r - 1)/(2r)) &= \end{aligned} \quad (60)$$

with  $r$  given by (25). Numerical solution of the critical condition (59) yields the curve  $f_{\text{sv,th}}(I)$  which is almost indistinguishable from the curve for  $f_{\text{sv}}^*$  from the full augmented system (Figure 9).

It is especially interesting to check the case  $I = 0$ . Then  $P = -Q'$  and the critical condition (59)–(60) simplifies to

$$\sin \left[ \pi f_{\text{sv,th}}^o + \left( f_{\text{sv,th}}^o - \frac{1}{2} \right) \frac{\pi(r - 1)}{2r} \right] = \cos(\pi f_{\text{sv,th}}^o) - 1, \quad (61)$$

which can be solved numerically to give  $f_{sv,th}^o \equiv f_{sv,th}(I = 0) = 0.1193$ , in agreement with numerical findings from previous dynamical simulations<sup>18</sup>.

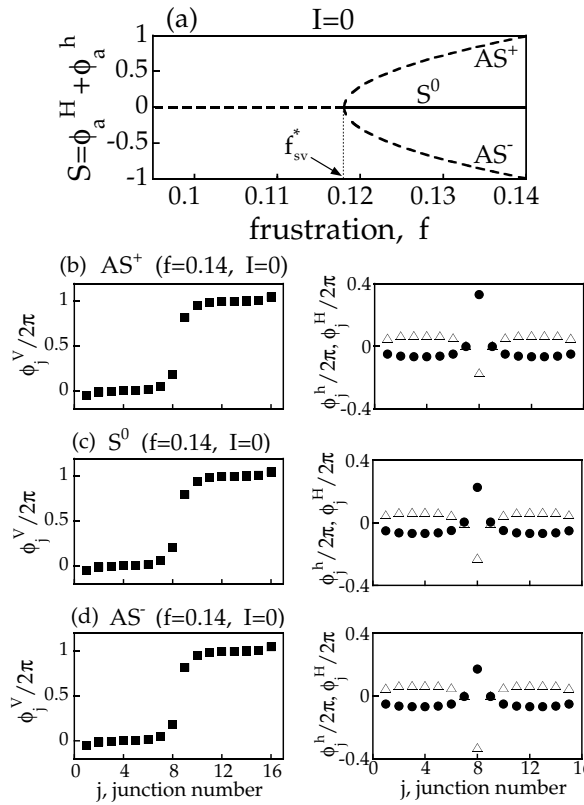


FIG. 11. Subcritical pitchfork bifurcation of the single-vortex solution at  $f_{sv}^*$ . (a) Value of the up-down asymmetry  $S = \phi_a^H + \phi_a^h$  for the two asymmetric ( $AS^+$ ,  $AS^-$ ) and symmetric ( $S^0$ ) branches with  $I = 0$ . The calculation of the dynamical eigenvalues (not shown) indicates that the stable symmetric branch becomes unstable at  $f_{sv}^*$  when it collides with the two unstable asymmetric branches. For  $f < f_{sv}^*$ , only the unstable symmetric branch survives. (b) Phases of the vertical (left) and horizontal (right) junctions for the asymmetric branch ( $AS^+$ ) at  $f = 0.14$  and  $I = 0$ . (c) and (d) are the same as (b) but for the  $S^0$  and the  $AS^-$  branches respectively. Note that although all three vertical configurations on the left panels look very similar, the (b) and (d) AS horizontal configurations on the right are up-down *asymmetric*.

### 3. Single-vortex configurations at the edges

So far we have concentrated on a particular single-vortex state, namely one where the vortex occurs in the middle cell of the array. But there are many other single-vortex states, each differing from the previous one by displacing the vortex by one cell to the right or to the left. Each of those configurations becomes unstable through bifurcations similar to those discussed above for the case

of the centered single-vortex state. For most values of  $f$ , as discussed in Section IV, when the driving current  $I$  is increased, a vortex in the ladder moves to the left (getting pinned in cells closer to the left edge as  $I$  grows) until it is expelled from the array at the left boundary. Thus, in explaining the effect of the edges on the sv solution we are most interested in two critical currents: the critical current  $I_{right}$ , at which a vortex at the right edge begins to move, and the critical current  $I_{left}$ , at which the vortex is expelled at the left edge of the ladder.

To predict  $I_{right}$ , we analyze the sv configuration with the vortex placed in the rightmost cell (the 000...01 configuration). The results of the analysis are similar to those for the vortex in the center. As shown in Figure 12(a), this state can cease to exist through a saddle-node bifurcation ( $I_{sv,right}^*$ ), or become unstable through a symmetry-breaking pitchfork bifurcation ( $f_{sv,right}^*$ ). The agreement with the dynamical simulations is excellent.

The rigorous explanation of  $I_{left}$  turns out to be slightly more complicated. A careful examination of the numerics reveals that, depending on the value of  $f$ , the vortex can be expelled from the array in one of two ways: from the leftmost cell (cell number 1) as expected, or directly from cell number 2. Thus, we need to examine the dynamical stability of two sv states: the one with the vortex in cell 1 (1000...00) and in cell 2 (0100...00).

The dynamic stability of the 0100...00 configuration contains no new elements. The two observed bifurcations (a saddle-node  $I_{sv,left2}^*$  and a subcritical pitchfork  $f_{sv,left2}^*$ ) are similar to those explained above. The results are presented in Figure 12(b) where the saddle-node bifurcation is seen to explain the dynamical  $I_{left}$  for  $f < 0.29$ .

However, it is the stability analysis of the 1000...00 state that explains the expulsion of the vortex at the edge for  $f > 0.29$ . As shown in Figure 12(c), this configuration presents the usual saddle-node ( $I_{sv,left1}^*$ ) bifurcation. The pitchfork ( $f_{sv,left1}^*$ ) bifurcation is barely visible in the figure. There is also another saddle-node bifurcation at low  $I$  and high  $f$  which is irrelevant for the depinning considered here.

The results of this section are summarized in Figure 12(d), which indicates the region where *at least one* single-vortex configuration in a ladder array *with edges* is dynamically stable. Figure 12(d) is, in essence, the union of Figure 9 with Figure 12(a)–(c) and shows how the sv solutions either cease to exist through a saddle-node bifurcation when  $I$  is increased for most values of the frustration  $f$ , or become unstable through a symmetry-breaking pitchfork bifurcation for small values of  $f$ .

Within this picture, the dynamical behavior in Figure 9, where the vortex propagates along the ladder in the interval  $I_{sv,right}^*(f) < I < I_{sv,left}^*(f)$ , is the result of a succession of saddle-node bifurcations of single-vortex states situated in contiguous cells until the vortex is expelled at the left edge. This is in contrast with the symmetry-breaking exit of the vortex for  $f < f_{sv}^*(I)$  where the flux

is expelled in the transversal direction.

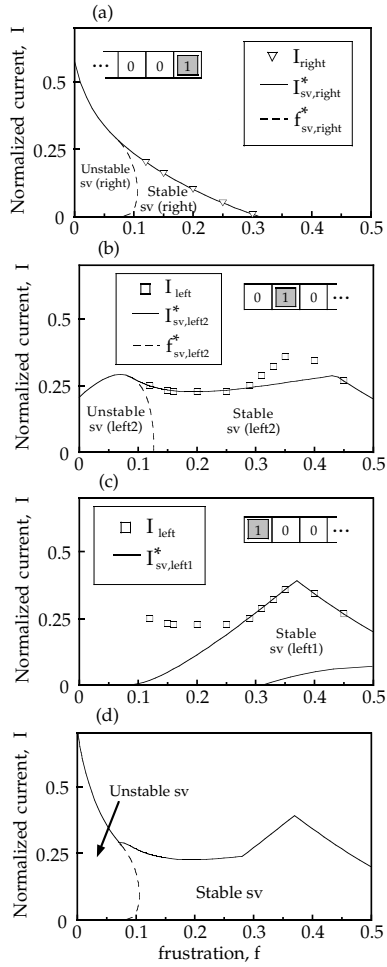


FIG. 12. (a)–(c) Stability diagrams for the sv configuration when the vortex is placed close to either edge. The symbols denote critical currents measured through dynamical simulations. The solid lines ( $I_{\text{sv}}^*$ ) correspond to saddle-node bifurcations and the dashed lines ( $f_{\text{sv}}^*$ ) to subcritical pitchfork bifurcations where the flux is expelled transversally. For instance, from (a) the vortex in the rightmost cell moves to the left for  $I > I_{\text{sv,right}}^*$ . And  $I_{\text{left}}$  corresponds to the expulsion of the vortex at the left edge for  $f < 0.37$ . In the region delimited by  $I_{\text{right}}$  and  $I_{\text{left}}$ , there is a cascade of saddle-node bifurcations which leads to the behavior observed in Figure 5. For the top three panels: (a) corresponds to the vortex in the rightmost cell; (b) in the second cell; and (c) in the first (leftmost) cell. (d) shows the region where at least one sv configuration (anywhere in the ladder) is stable. It is the union of panels (a)–(c) and Figure 9.

This description is valid for  $f < 0.37$ . However, a subtle variation is observed beyond that point for the sv solutions. The comparison of Figure 12(c) and Figure 8 shows that the depinning of the sv and nv states is similar for high  $f$ , i.e.  $I_{\text{sv,left}}^* \approx I_{\text{nv}}^*$ , for  $f > 0.37$ . This is due to the fact that at high  $f$  the vortex is *not* expelled from

the array before depinning. Instead, the sv configuration with the vortex at the left edge ceases to exist through a saddle-node bifurcation which, similarly to what happens to the nv state, is localized on the *right* edge of the ladder. The depinning transition of the single-vortex state at high  $f$  can be described in a similar fashion as the depinning of the no-vortex configuration: by the nucleation of vortices on the right edge of the ladder. Thus, the single-vortex configuration plays no role in the global depinning of the array: only the behavior of the nv and ff states has to be considered.

### C. Bifurcations of the fully-frustrated state

The depinning of the ladder array as  $f \rightarrow 1/2$  is determined by the stability of the fully-frustrated configuration. This can be readily seen by inspection of Figure 6 which shows that at high  $f$  the depinning of the no-vortex state occurs *before* the global depinning of the array.

To clarify the importance of these transitions we follow the same scheme as above. We first calculate the zero-eigenvalue bifurcations of this state and show that the depinning of the ladder at  $f \simeq 1/2$  is indeed explained by a saddle-node bifurcation of the ff state. Then we obtain analytical approximations (“th”) to the exact bifurcations, using stability criteria for the infinite-ladder ff configuration.

In principle, the characterization of the ff bifurcations is more intricate than for the nv and sv configurations above since in the *finite* ladder several states of the ff type could play a role in the depinning. First, there exist different states in ladders with odd and even number of cells, as seen when the ...010101... alternating vortex pattern is fitted into a finite length. Second, there are many ff-states very close energetically with different dynamic stability structure. However, we will show that the landscape of relevant solutions is indeed clear, and depinning can be assigned to instabilities of *one* of those configurations.

Consider first an *even* ladder with ten plaquettes as an example. Of the several states of the ff type, three can be thought as relevant: (1a) 1010101010, (1b) 0101010101, and (1c) 1101010100. We have analyzed the stability of these three states and conclude that only configuration (1a) is relevant for depinning of the even ladder. Both (1b) and (1c) cease to exist or become unstable at lower critical currents. This is physically reasonable since (1b) will tend to move one cell to the left under the action of a driving current to produce (1a), while (1c) ceases to exist through a low current saddle-node bifurcation caused by the expulsion of the vortex at the left boundary.

The case of the *odd* ladder with  $N$  plaquettes has one further complication, namely that we cannot have exactly  $N/2$  vortices in the array. Thus, the “pure” ff state (as calculated for the infinite case) is not possible under these topological constraints. However, states simi-

lar to the “pure” ff are those which contain  $(N - 1)/2$  and  $(N + 1)/2$  vortices. Take, for instance, a ladder with eleven plaquettes. We have then two groups of states: those with 6 vortices, (2a) 10101010101, (2b) 11010101010, and (2c) 01010101011; and those with 5 vortices, (3a) 10101010100, (3b) 01010101010, and (3c) 00101010101. The detailed analysis of these states shows that (3a) has the highest critical transition and is thus responsible for the depinning of the odd ladder.

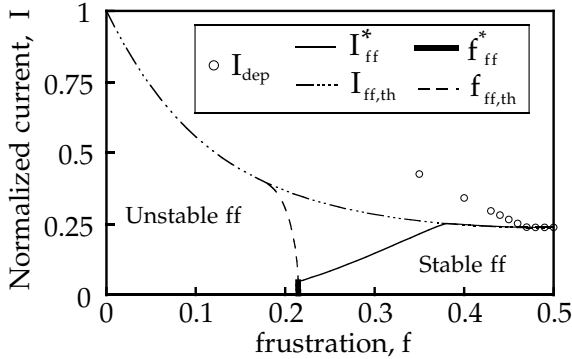


FIG. 13. Dynamic stability of the fully-frustrated solution. The saddle-node bifurcation at  $I_{\text{ff}}^*$  is responsible for the depinning of the array for  $f \sim 0.5$ . The ff state also undergoes a pitchfork bifurcation  $f_{\text{ff}}^*$ . Both are partially explained through approximate formulas  $I_{\text{ff},\text{th}}$  and  $f_{\text{ff},\text{th}}$  deduced from instabilities of the ff solution for the *infinite* ladder.

There is a final important observation in our argument: the stability diagrams of the configurations which cause the depinning in odd and even ladders –(3a) and (1a) respectively– are *indistinguishable*. (This is also true for other odd-even related configurations like (2b) and (1c).) The conclusion is then clear: the depinning behavior of odd and even ladders at high  $f$  is identical as it can be explained by the bifurcation of configurations (1a) and (3a) which are of the 101010... type.

The zero-eigenvalue bifurcations of these configurations are presented in Figure 13. The bifurcations are of two types (similar to those obtained for the sv state): saddle-node ( $I_{\text{ff}}^*$ ) and pitchfork ( $f_{\text{ff}}^*$ ). Note also how the saddle-node bifurcation corresponds to two distinct dynamical instabilities: for  $0.38 < f < 0.5$ , the instability is spatially extended, while for  $0.22 < f < 0.38$ , the instability is localized at the *right* edge. Only the former (spatially extended) saddle-node bifurcation has any relevance for the global depinning of the array—as reflected by the agreement between  $I_{\text{dep}}$  and  $I_{\text{ff}}^*$  for  $f > 0.45$ . (Of course, for  $f < 0.45$ , the depinning current and  $I_{\text{ff}}^*$  no longer coincide, because the depinning is caused there by a saddle-node bifurcation of a different state, the no-vortex solution, as shown earlier.) The pitchfork bifur-

cation  $f_{\text{ff}}^*$  is also spatially extended and, as observed for the single vortex, it implies the breaking of the up-down symmetry in the ff state. Thus, the flux is expelled in the transversal direction. We clarify this in the following by calculating some analytical approximations to these criteria.

### 1. Analytical approximations to the ff bifurcations

The rigorous analysis above indicates that two of the bifurcating mechanisms imply spatially extended perturbations which are not localized at the edges. Hence, we turn to instabilities of the infinite-ladder fully-frustrated solution to obtain analytical approximations.

One of the criteria was already established in Section III where we showed that the no-edge ff solution ceases to exist at a current  $I_{\text{ff},\text{th}}(f)$  given by (40). Indeed, we find excellent numerical agreement between the analytical  $I_{\text{ff},\text{th}}$  and the numerical  $I_{\text{ff}}^*$  for  $0.38 < f < 0.5$  (Figure 13). For instance, the predicted  $I_{\text{ff},\text{th}}(f = 1/2) = \sqrt{5} - 2 = 0.236$  is very close to the dynamically computed  $I_{\text{dep}}(f = 1/2) = 0.238$ .

To explain the observed pitchfork bifurcation, recall that the up-down symmetric manifold of solutions becomes unstable to normal perturbations when the absolute value of the horizontal phases is larger than  $\pi/2$ , as given in (11). Thus, from (34)–(39) and the critical condition  $|\phi^{H^\dagger}| = \pi/2$  we obtain the following implicit equation for the instability boundary  $f_{\text{ff},\text{th}}(I)$ :

$$I = \tan(\pi f_{\text{ff},\text{th}}) \sqrt{\cos^2(\pi f_{\text{ff},\text{th}}) - 4 \sin^4(\pi f_{\text{ff},\text{th}})}, \quad (62)$$

which is shown in Figure 13 and compared to the exact  $f_{\text{ff}}^*$  with excellent agreement. As an example, it is easy to show analytically that the value of this critical field when  $I = 0$  is given by

$$f_{\text{ff},\text{th}}(I = 0) = \frac{1}{\pi} \arcsin \left[ \sqrt{\frac{17^{1/2} - 1}{8}} \right] = 0.2148. \quad (63)$$

In summary, we can explain in part the stability diagram of the ff state in the presence of edges with two bifurcations of the infinitely extended (no-edge) ff solution: the saddle-node bifurcation  $I_{\text{ff},\text{th}}(f)$ , and the subcritical pitchfork  $f_{\text{ff},\text{th}}(f)$ .

However, for the finite ladder, another saddle-node bifurcation is reached before  $I_{\text{ff},\text{th}}$  for  $0.22 < f < 0.38$  as seen in Figure 13. Numerical analysis shows that this bifurcation is local and it corresponds to an instability in the *leftmost* cell. It can be approximated heuristically by a criterion similar to (56) for the nv state, i.e. for this interval of the frustration the ff state depins approximately when the leftmost junction becomes unstable.

## VI. SUMMARY AND DISCUSSION

The first conclusion of our analysis is that for most values of  $f$ , the global depinning current of the array  $I_{\text{dep}}(f)$  coincides with the current  $I_{\text{nv}}^*$  where the no-vortex state undergoes a saddle-node bifurcation (Figure 6). This bifurcation point can be well approximated by an analytical  $I_{\text{nv,th}}$ , given in (58), derived from an instability criterion for the rightmost junction of the array. For values of  $f$  close to  $1/2$ , however, the global depinning is caused by a saddle-node bifurcation of the fully-frustrated solution at a current  $I_{\text{ff}}^*$ . This bifurcation itself is well approximated by the global instability of the no-edge ff state at  $I_{\text{ff,th}}$ , as given analytically in equation (40).

We have also shown that the depinning of the single vortex and its subsequent motion in the  $-\hat{x}$  direction (Figure 5) is the result of a cascade of saddle-node bifurcations of the single-vortex solution such that, for most values of  $f$ , the fluxoids are expelled from the ladder through its left edge. More surprisingly, for smaller  $f$  the sv and ff configurations can also undergo another transition: a symmetry-breaking subcritical pitchfork bifurcation in which the up-down symmetry of the horizontal phases plays a crucial role. In this case, the fluxoids are expelled in the transversal ( $-\hat{y}$ ) direction through the horizontal junctions.

At a finer level of description, the approximations obtained in Section III for the nv, ff and sv states all have a common feature: the corrections due to the existence of edges, or of topological vortices in the array, decay exponentially in space with a characteristic length dependent on  $I$  and  $f$ , as seen in (25) for instance. Thus, the effect of the perturbations can usually be captured by a local analysis. This explains why, besides their independence from the purely dynamical parameter  $\beta_c$ , the depinning observables are largely independent of  $N$ , the length of the array.

We have summarized our results in a zero-temperature stability diagram (Figure 14) where we present the different critical currents for the nv, sv, and ff superconducting solutions for the *finite* ladder (with edges). In short, the array ceases to be superconducting (depins globally) at  $I_{\text{dep}}$  when either the no-vortex, single-vortex or fully-frustrated solutions ceases to exist through saddle-node bifurcations.

The presence of vortices in the array does not change the observed depinning. If  $f < f_{\text{min}}(I) \sim 0.1$ , the single-vortex solution is always unstable. For  $f_{\text{min}} < f < 0.37$ , a vortex in the array will depin at  $I_{\text{LAT}} < I_{\text{dep}}$  and will be expelled at the left edge at  $I_{\text{left}} < I_{\text{dep}}$ . At that point the no-vortex solution is recovered. This behavior is the same for multivortex solutions with moderate  $f$ . For  $f > 0.37$ , the single-vortex is not expelled at the left edge before depinning but its instability is almost identical to that of the no-vortex configuration since vortices enter from the right edge.

Note that no energy criteria have been invoked above.

The calculation of energy boundaries for the relevant states remains open for further investigation.

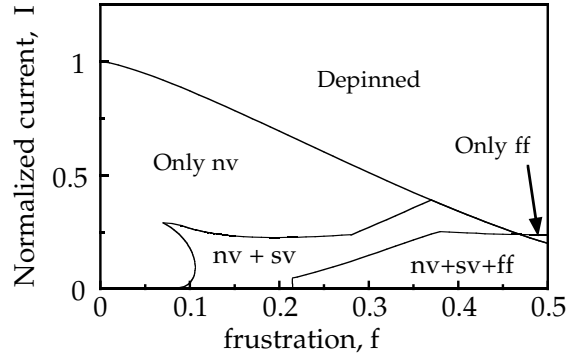


FIG. 14. Dynamic stability diagram in the finite ladder (with edges) of the superconducting states analyzed in this paper: the no-vortex (nv), fully-frustrated (ff), and single-vortex (sv) configurations. This figure combines Figures 8, 12(d), and 13. Labels indicate the states that are *dynamically* stable inside each region. In regions where two or more stable states coexist, each is attained from different initial conditions.

To highlight the effect of the edges and to include energetic considerations we explore in more detail the phase diagram for the infinite ladder (no edges), which we present in Figure 15. (This should be compared to the phase diagram of the ladder with edges in Figure 14.) When no edges are present, the dynamic bifurcation boundaries for the three states are given by  $I_{\text{nv,th}}^\dagger$ ,  $I_{\text{ff,th}}^\dagger$ ,  $f_{\text{ff,th}}^\dagger$ ,  $I_{\text{sv,center}}^*$ , and  $f_{\text{sv,center}}^*$ . These dynamic criteria do not contradict previous thermodynamic studies of the infinite ladder<sup>13,14</sup> with  $I = 0$  where the no-vortex solution was calculated to be energetically stable only for frustrations smaller than a thermodynamic critical field  $f_{c1}$ , above which the flux penetrates the ladder. We have extended these calculations for the *driven* infinite ladder and the three superconducting solutions addressed in this article. Defining the energy of a given configuration as

$$E = - \sum_{\text{all}} \cos \phi_j,$$

we have calculated the energy boundaries for the approximate no-edge no-vortex, fully-frustrated and single-vortex solutions:  $f_{\text{nv-sv}}(I)$ ,  $f_{\text{nv-ff}}(I)$  and  $f_{\text{sv-ff}}(I)$ . The results of these *thermodynamic* calculations are also presented in Figure 15. Note, for instance, that our calculated  $f_{c1} = f_{\text{nv-sv}}(I = 0) \simeq 0.282$  agrees well with other estimates<sup>14</sup>  $f_{c1} \simeq 2\sqrt{2}/\pi^2 = 0.287$ .

Moreover, our approximate solutions produce some new analytical results. For example, a closed expression for the energy boundary between the no-vortex and fully-frustrated solutions  $f_{\text{nv-ff}}(I)$  can be obtained as:

$$\begin{aligned} \sqrt{1 - I^2} - I \sqrt{2/L - 1} + 2 \cos(\pi f_{\text{nv-ff}}) \\ - 2 \sin(\pi f_{\text{nv-ff}}) \sqrt{1 - 2I^2/L} = 0 \end{aligned} \quad (64)$$

where  $L$  is given by (39) with the negative sign. For the special case  $I = 0$ , and using the limit  $2I^2/L \rightarrow (1 + 4 \sin^2 \pi f)^{-1}$ , it can be shown analytically that this boundary crosses the  $I = 0$  axis at  $f_{\text{nv-ff}}(I = 0) = 1/3$ .

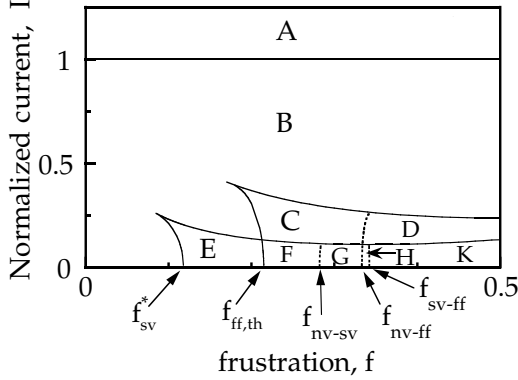


FIG. 15. Phase diagram of the infinite ladder (no edges) for the nv, sv and ff solutions. It can also be used to describe the ring ladder. Solid lines are the dynamical critical currents derived in the previous sections for solutions with no edges and for the vortex in the center of the array. Dashed lines indicate the thermodynamic boundaries where the energies of the approximate solutions are equal. The physical meaning of the different regions can be summarized as follows: A: Running solution (no superconducting solution exists); B: Only nv exists, and it is stable; C:  $E_{\text{nv}} < E_{\text{ff}}$ ; D:  $E_{\text{ff}} < E_{\text{nv}}$ ; E:  $E_{\text{nv}} < E_{\text{sv}}$ ; F:  $E_{\text{nv}} < E_{\text{sv}} < E_{\text{ff}}$ ; G:  $E_{\text{sv}} < E_{\text{nv}} < E_{\text{ff}}$ ; H:  $E_{\text{sv}} < E_{\text{ff}} < E_{\text{nv}}$ ; K:  $E_{\text{ff}} < E_{\text{sv}} < E_{\text{nv}}$ . The dotted lines  $f_{\text{nv-sv}}$ ,  $f_{\text{nv-ff}}$  and  $f_{\text{sv-ff}}$  are approximate thermodynamical criteria. In particular,  $f_{\text{nv-sv}}$  is analogue to the  $f_{c1}$  defined by Kardar<sup>14</sup> and  $f_{\text{nv-sv}}(I = 0) = 0.2823$  is in good agreement with his estimate. Moreover, the zero-current energy boundary between the nv and ff solutions (64) can be shown analytically to occur at  $f_{\text{nv-ff}}(I = 0) = 1/3$ . On the other hand, both  $f_{\text{sv}}^*$  and  $f_{\text{ff,th}}$  ensue from dynamical instability conditions. For  $I = 0$ ,  $f_{\text{sv}}^*$  can be approximated by  $f_{\text{sv,th}}(I = 0) = 0.1193$ , as given by (61), explaining the numerical observations of Hwang *et al.*<sup>18</sup> for  $f_{c1\perp}$ . Another analytical result (63) shows that  $f_{\text{ff,th}}(I = 0) = 0.2148$ .

We emphasize also that the regions in Figure 15 present distinct dynamical and thermodynamical stabilities. For instance, in some of them, the single-vortex solution is not the ground state of the system, although it is *dynamically* stable (metastable).

When comparing our results with those found in earlier work, one should carefully note the direction of injection of the driving current  $I$ . Previous analytical studies<sup>14,15</sup> have focused on the  $I = 0$  case and considered the effect of a small *parallel* current in the  $\hat{x}$  direction. In contrast,

here  $I$  is injected in the *perpendicular* ( $\hat{y}$ ) direction. The depinning depends on the direction of current injection, a factor to be taken into account when explaining recent numerical simulations of ladder arrays<sup>18</sup>. In those simulations, marked differences between the depinning current of a circular ladder with *perpendicular* injection, and of an open-ended ladder with *parallel* injection were reported.

Although we have not studied the ring ladder in this paper, it is closely connected to the infinite (no-edge) ladder. The solutions for the infinite ladder constitute a sub-manifold of the solutions for the ring ladder (i.e., the topological constraints are more strict on the infinite ladder than in the ring ladder). To understand this, note first that the governing equations (12)–(14) are the same for both ring and infinite ladders. On the other hand, following the same reasoning given by the sequence of equations (3)–(9), we conclude that the topological constraints in the ring ladder imply only that

$$I_j^H + I_j^h = C, \quad \forall j, \quad (65)$$

where  $C$  is a constant. Therefore, from (9), the infinite ladder is mathematically equivalent to the particular case of the ring with  $C = 0$ , in which the concentric currents through the horizontal junctions in the outer  $I^H$  and inner  $I^h$  circles are equal and opposite.

Consequently, the results for the infinite ladder summarized in Figure 15 are also valid for the ring ladder if we restrict to the submanifold with  $C = 0$ . In this case, the phase diagram has to be reinterpreted in terms of the new topological constraints. First, the depinning of the no-vortex solution is unchanged:  $I_{\text{nv,th}}^\dagger$  is still constant and equal to 1. However, the two bifurcations of the single-vortex configurations have new dynamical meaning. If the sv state goes unstable through the saddle-node bifurcation  $I_{\text{sv}}^* = I_{\text{LAT}}$ , flux cannot be expelled through the horizontal junctions and the vortex depins and moves along the ladder circularly. Thus, the ring ladder depins effectively at  $I_{\text{LAT}}$ . However, if  $f < f_{\text{sv}}^*$ , the flux can be expelled *transversally* from the ladder through the horizontal junctions and the no-vortex state is recovered. Then, the depinning occurs at  $I_{\text{nv,th}}^\dagger = 1$ . This is exactly the behavior reported from numerical simulations by Hwang *et al.*<sup>18</sup>. First, their isotropic  $I_{c\perp}$  coincides with our calculated  $I_{\text{sv}}^* = I_{\text{LAT}}$ . Second, they found a critical field  $f_{c1\perp}^* \simeq 0.12$  below which the depinning current is  $I_{c\perp} = 1$  with exclusion of field inside the array. This corresponds to  $f_{\text{sv}}^*$ , the frustration below which the single-vortex configuration becomes dynamically unstable through a symmetry-breaking pitchfork bifurcation, which can be approximated analytically by  $f_{\text{sv,th}}(I)$ , as given in (59). (In the absence of driving, the analytical prediction (61) gives  $f_{\text{sv,th}}(I = 0) = 0.1193$ , in perfect agreement with their numerical simulations<sup>18</sup>.)

We note in passing that the same behavior should be expected for the fully-frustrated state in the ring ladder. The checkerboard pattern would begin to slide along the

ring at  $I_{ff,th}$  producing a finite voltage. However, if the  $f_{ff,th}$  is crossed, the flux can be expelled transversally and the nv state would appear. These predictions would have to be checked numerically.

As a final remark, we also note that the second device considered by Hwang *et al.*<sup>18</sup>—an open-ended ladder with *parallel* current injection—cannot be compared directly with our ladder with *perpendicular* injection. However, the depinning current  $I_c(f)$  follows a similar trend to our  $I_{dep}(f)$ . In fact, the dependence of their  $I_c(f)$  seems to be well explained with formulae calculated by Benedict<sup>15</sup> for the same device by invoking a similar criterion: the onset of soft modes<sup>29</sup>.

## ACKNOWLEDGMENTS

We thank Shinya Watanabe, Enrique Trías, and Herre van der Zant for consistently useful discussions, and Mehran Kardar for helpful guidance to the literature on ladder arrays. Research supported by a Spanish MEC-Fulbright predoctoral fellowship (MB), and by NSF grants DMS-9500948 (SHS) and DMR-9402020 (TPO).

## APPENDIX A: COMPARISON OF THE SINGLE-VORTEX CONFIGURATION IN THE LADDER WITH THE ONE-DIMENSIONAL KINK

Although analogies between the ladder and strictly one-dimensional parallel arrays can be drawn, we show now how the single-vortex solution for the quasi-one-dimensional ladder is mathematically different from the kink-like vortex in 1-D parallel arrays.

Recall that the equations for the one-dimensional parallel array can be reduced to a discrete driven sine-Gordon equation<sup>7,23</sup> if only self-inductances are considered. When  $I = 0$ , the discrete single-vortex solution is well approximated by the kink solution of the undriven, time-independent, infinitely-extended, one-dimensional continuum sine-Gordon equation<sup>30</sup>:

$$\phi_i^{\text{SG}} = 4 \arctan\{\exp[(i - i_0)/\lambda_{\text{SG}}]\}. \quad (\text{A1})$$

Thus, the vortex corresponds to a  $2\pi$ -jump centered at  $i_0$  with a characteristic half-width  $\lambda_{\text{SG}}$ . (Incidentally, it has also been shown<sup>23</sup> that by introducing an effective  $\lambda_{\text{SG}}^{\text{eff}}$ , this functional form is also valid when mutual inductances are included).

For our no-inductance ladder array, it is also possible to obtain an approximate sine-Gordon equation for the system. Although there is no explicit inductance in the problem, the coupling between the vertical junctions is provided by the horizontal junctions via the fluxoid quantization.

The approximate sine-Gordon equation has been most simply obtained<sup>14,19</sup> by assuming that the horizontal phases are small:  $\sin \phi_j^H \approx \phi_j^H$ . Then, the *zero-current*

time-independent equations for the ladder (15)–(16) can be reduced to  $\phi_{j+1}^V - 2\phi_j^V + \phi_{j-1}^V = 2 \sin \phi_j^V$ . This gives, in the continuum limit, the time-independent sine-Gordon equation with no forcing and  $\lambda_{\text{SG}} = 1/\sqrt{2}$ , where the cell size is taken as length unit. However, a better linearization is suggested by the numerics if we take the phase change in the vertical junctions  $(\phi_j^V - \phi_{j+1}^V)/2 = \phi_j^H - \pi f \ll 1$  as the small parameter. In other words, one should linearize about  $\phi_j^H = \pi f$ , not  $\phi_j^H = 0$ . In that case, we obtain the following more accurate sine-Gordon equation:  $\phi_{xx}^V - (2/\cos \pi f) \sin \phi^V = 0$ , with  $\lambda_{\text{SG}}^2 = \cos(\pi f)/2$ .

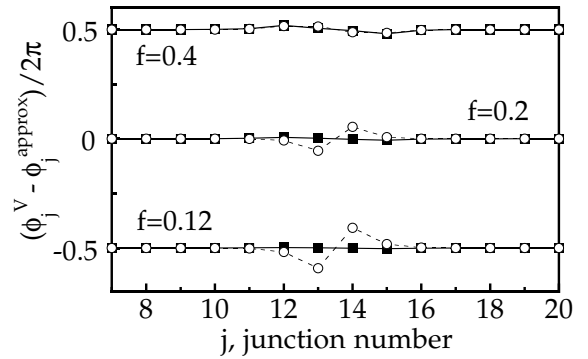


FIG. 16. Comparison of the errors of our approximation (30) (black squares) and the sine-Gordon kink (A1) (white circles) for varying magnetic field far from the edges in a  $25 \times 1$  array. Graphs for different  $f$  are offset by  $\pi$  for clarity. The approximation (30) has no adjustable parameters. In contrast, to make the kink approximation as accurate as possible, its characteristic length  $\lambda_{\text{SG}}$  was chosen by a linear fit of  $\ln[\tan(\phi_j^V/4)]$  vs.  $j$ , where the  $\phi_j^V$  are the numerically computed phases of the true single-vortex state. Even with this *a posteriori* fit to the numerical data, the kink is not as good an approximation as (30).

We argue now that the numerically observed single-vortex configuration is not as accurately approximated by the kink (A1) as it is by our expression (30)–(32). To compare them, we particularize (30)–(32) for  $I = 0$  for a long array such that  $1 \ll a \ll N + 1$ . Then, the vertical phases near the center of the vortex become

$$\phi_j^V = \begin{cases} P \exp\{(j - a)/\lambda\}, & j \leq a \\ 2\pi - P \exp\{(a + 1 - j)/\lambda\}, & j > a \end{cases} \quad (\text{A2})$$

with  $r$  and  $\lambda$  given by (25) and  $P$  by

$$\sin P = \sin\left(\pi f - \frac{r-1}{2r}P\right) + \sin(\pi f + P). \quad (\text{A3})$$

Note that in (A2) we have not reduced the phases to the interval  $[-\pi, \pi]$ , to facilitate the comparison with (A1).

Our solution resembles the sine-Gordon kink in that it describes a  $2\pi$ -jump with odd symmetry with respect to  $x_0 = a + 1/2$ . However, both the functional forms and the characteristic lengths are different. Figure 16 shows that the numerics are better approximated over a wide range of  $f$  by (A2) than by the sine-Gordon kink (A1).

Given the relative inappropriateness of the sine-Gordon kink as a model of the vortex in the no-inductance ladder array, we conclude that even for the static case it is an oversimplification to reduce the ladder to a one-dimensional parallel array where the horizontal junctions are approximated by an effective inductance. Other dynamic phenomena observed in the ladder, e.g., the dynamical mechanism of retrapping from the whirling mode, reinforce this statement and will be discussed elsewhere<sup>21</sup>.

## APPENDIX B: NO-VORTEX SOLUTION AND DEPINNING WITH SELF-INDUCTANCE

Following on the concepts and notation in Sections III and IV, we briefly consider the ladder with self-inductance. This is a first approximation to explore the effect of self-fields on the no-vortex solution and, consequently, on the global depinning current of the array.

When self-inductances are included, the time-independent governing equations (15)–(16) become

$$I + \sin \phi_{j-1}^H = \sin \phi_j^H + \sin \phi_j^V \quad (B1)$$

$$\phi_j^V - \phi_{j+1}^V - 2\phi_j^H = 2\pi(n_j - f) - I_j^m/\Lambda^2, \quad (B2)$$

where  $I_j^m$  is the mesh current in plaquette  $j$  and  $\Lambda^2 = L_J/L_s$  is the two-dimensional penetration depth and a measure of the discreteness of the array. Due to the geometrical constraints of the ladder, it is readily seen that  $I_j^m = -I_j^H$  in this case.

For the no-vortex solution we still have  $\phi_j^V \simeq \phi_{j+1}^V = \phi^{V*}$  and  $\phi_j^H \simeq \phi_{j+1}^H = \phi^{H*}$  far from the edges. From (B1) we then get

$$\phi^{V*} = \arcsin I, \quad (B3)$$

as for the case with no inductance ( $\Lambda = \infty$ ). However, the horizontal phase is different and has to be calculated from the following nonlinear equation:

$$\phi^{H*} + \frac{1}{2\Lambda^2} \sin \phi^{H*} = \pi f. \quad (B4)$$

This is a particular case of Kepler's equation, studied in celestial mechanics<sup>31</sup>, which can be solved through the method of successive approximations. In our case, a good approximation to  $\phi^{H*}$  over the whole range of  $f$  is given by the first iteration of that method as:

$$\phi^{H*} \simeq \pi f - \frac{1}{2\Lambda^2} \sin \left( \frac{2\Lambda^2}{1 + 2\Lambda^2} \pi f \right).$$

The procedure to account for the open boundaries is identical to that presented in Section III. The results are also similar: the corrections decay exponentially from the edges as in (23)–(25). However, the characteristic length  $\lambda_s = 1/\ln r_s$  is now given by  $r_s = \alpha_s + \sqrt{\alpha_s^2 - 1}$  where

$$\alpha_s = 1 + \frac{\sqrt{1 - I^2}}{\cos \phi^{H*}} \left( 1 + \frac{1}{2\Lambda^2} \cos \phi^{H*} \right). \quad (B5)$$

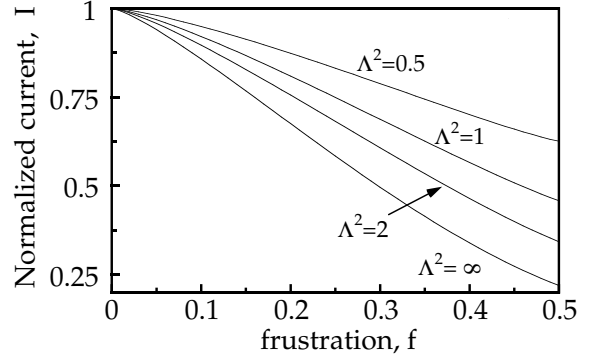


FIG. 17. Effect of the self-inductance on the depinning current. We show how the heuristic depinning approximation  $I_{\text{nv,th}}(f)$ , obtained from (B6), varies with the self-inductance  $\Lambda^2 = L_J/L_s$ . Note that the rest of the paper deals with the limiting case  $\Lambda = \infty$  where all inductances are neglected.

To assess how the inductance affects the depinning current, we use (B5) and the  $\phi^{H*}$  obtained from (B4) with a heuristic criterion similar to (58),

$$\arcsin(1 - I_{\text{nv,th}}) = \phi^{H*} - \frac{r_s - 1}{2r_s} \arccos I_{\text{nv,th}}, \quad (B6)$$

to calculate  $I_{\text{nv,th}}(f, \Lambda^2)$ . The results in Figure 17 show that, for fixed  $\Lambda$ ,  $I_{\text{nv,th}}(f)$  still decreases monotonically with  $f$ . However, for a given  $f$ , the value of the depinning current increases as  $\Lambda$  diminishes. This is expected on physical grounds since an increase in the inductance  $L_s$  implies larger self-fields which oppose the external applied magnetic field, thus decreasing the effective magnetic flux through the array.

<sup>1</sup> K.K. Likharev, *Dynamics of Josephson Junctions and Circuits*, (Gordon and Breach, New York, 1986); T. van Duzer and C.W. Turner, *Principles of Superconductive Devices and Circuits* (Elsevier, New York, 1981); M. Tinkham, *Introduction to Superconductivity* (2<sup>nd</sup> ed.) (McGraw-Hill,

New York, 1996); T.P. Orlando and K.A. Delin, *Foundations of Applied Superconductivity*, (Addison-Wesley, Reading, MA, 1991).

<sup>2</sup> P.A.A. Booij and S.P. Benz, *Appl. Phys. Lett.* **64**, 2163 (1994); S.P. Benz and C.A. Hamilton, *Appl. Phys. Lett.* **68**, 3171 (1996).

<sup>3</sup> R. Kleiner *et al.*, *Phys. Rev. Lett.* **68**, 2394 (1992); R. Kleiner *et al.*, *Phys. Rev. B* **50**, 3942 (1994).

<sup>4</sup> R.A. Hyman *et al.*, *Phys. Rev. B* **51**, 15304 (1995).

<sup>5</sup> P. Hadley, M.R. Beasley, and K. Wiesenfeld, *Phys. Rev. B* **38**, 8712 (1988); A.A. Chernikov and G. Schmidt, *Phys. Rev. E* **52**, 3415 (1995); K. Wiesenfeld, P. Colet, and S.H. Strogatz, *Phys. Rev. Lett.* **76**, 404 (1996); S. Watanabe and J. Swift, *J. Nonlinear Sci.*, to be published.

<sup>6</sup> S. Watanabe and S.H. Strogatz, *Physica* (Amsterdam) **74D**, 197 (1994).

<sup>7</sup> H.S.J. van der Zant *et al.*, *Phys. Rev. Lett.* **74**, 174 (1995); S. Watanabe *et al.*, *Phys. Rev. Lett.* **74**, 379 (1995); S. Watanabe *et al.*, *Physica* (Amsterdam) **97D**, 429 (1996).

<sup>8</sup> A good sample of current research is presented in *Macroscopic Quantum Phenomena and Coherence in Superconducting Networks*, ed. C. Giovanella and M. Tinkham (World Scientific, Singapore, 1995). See also *Physica* (Amsterdam) **222B**(4), 253-406 (1996).

<sup>9</sup> M. Kardar and D. Ertaş in *Scale Invariance, Interfaces, and Non-Equilibrium Dynamics*, NATO ASI Series (Plenum, New York, 1995).

<sup>10</sup> S.H. Strogatz, *Nonlinear Dynamics and Chaos: With Applications to Physics, Biology, Chemistry, and Engineering* (Addison-Wesley, Reading, MA, 1994), specially pp. 241-253.

<sup>11</sup> J.S. Chung, K.H. Lee, and D. Stroud, *Phys. Rev. B* **40**, 6570 (1989); F. Falo, A.R. Bishop, and P.S. Lomdahl, *Phys. Rev. B* **41**, 10983 (1990); D. Reinel *et al.*, *Phys. Rev. B* **49**, 9118 (1994); J.R. Phillips, H.S.J. van der Zant, and T.P. Orlando, *Phys. Rev. B* **50**, 9380 (1994); D. Domínguez and J.V. José, *Mod. Phys. B* **8**, 3749 (1994).

<sup>12</sup> I.F. Marino and T.C. Halsey, *Phys. Rev. B* **50**, 6289 (1994); A.S. Landsberg, Y. Braiman, and K. Wiesenfeld, *Phys. Rev. B* **52**, 15458 (1995); G. Filatrella and K. Wiesenfeld, *J. Appl. Phys.* **78**, 1878 (1995); I.F. Marino, *Phys. Rev. B* **52**, 6775 (1995); I.F. Marino, *Phys. Rev. B* **55**, 551 (1997); M. Barahona *et al.*, *Phys. Rev. B* **55**, R11989 (1997).

<sup>13</sup> M. Kardar, *Phys. Rev. B* **30**, 6368 (1984).

<sup>14</sup> M. Kardar, *Phys. Rev. B* **33**, 3125 (1986).

<sup>15</sup> K.A. Benedict, *J. Phys.: Condens. Matter* **1**, 4895 (1989).

<sup>16</sup> J.J. Mazo, F. Falo, and L.M. Floría, *Phys. Rev. B* **52**, 10433 (1995).

<sup>17</sup> C. Denniston and C. Tang, *Phys. Rev. Lett.* **75**, 3930 (1996).

<sup>18</sup> I-J. Hwang, S. Ryu, and D. Stroud, *Phys. Rev. B* **53**, R506 (1996).

<sup>19</sup> S. Ryu, W. Yu, and D. Stroud, *Phys. Rev. E* **53**, 2190 (1996); W. Yu, E.B. Harris, S.E. Hebboul, J.C. Garland, and D. Stroud, *Phys. Rev. B* **45**, 12624 (1992).

<sup>20</sup> M. Barahona, Ph.D. Thesis (MIT, June 1996).

<sup>21</sup> M. Barahona, S.H. Strogatz, and T.P. Orlando, to be published.

<sup>22</sup> J.F. Heagy, T.L. Carroll, and L.M. Pecora, *Phys. Rev. E* **50**, 1874 (1994); E. Ott and J.C. Sommerer, *Phys. Lett.* **A 188**, 39 (1994); P. Ashwin, J. Buescu, and I. Stewart, *Phys. Lett. A* **193**, 126 (1994); Y.-C. Lai and C. Grebogi, *Phys. Rev. E* **52**, R3313 (1995); P. Ashwin, J. Buescu, and I. Stewart, *Nonlinearity* **9**, 703 (1996); L. Kocarev and U. Parlitz, *Phys. Rev. Lett.* **76**, 1816 (1996); R. Brown and N.F. Rulkov, *Chaos* (submitted).

<sup>23</sup> H.S.J. van der Zant, E.H. Visscher, D.R. Curd, T.P. Orlando, and K.A. Delin, *IEEE Trans. Appl. Supercond.* **3**, 2658 (1993); R.D. Bock, J.R. Phillips, H.S.J. van der Zant, and T.P. Orlando, *Phys. Rev. B* **49**, 10009 (1994).

<sup>24</sup> The other solution for (34)–(37) at  $I = 0$ ,  $\{\phi_j^{V\dagger} = \pi/2 [1 + (-1)^j], \phi_j^{H\dagger} = 0\}$  is unstable and not a ground state of the system.

<sup>25</sup> C.J. Lobb, D.W. Abraham, and M. Tinkham, *Phys. Rev. B* **27**, 150 (1983).

<sup>26</sup> H.S.J. van der Zant, T. P. Orlando, and J.E. Mooij, *Phys. Rev. B* **43**, 10218 (1991).

<sup>27</sup> M. Barahona and S.H. Strogatz, to be published.

<sup>28</sup> W. Kaplan, *Advanced Calculus* (Addison-Wesley, Reading, MA, 1984), pp. 117-120.

<sup>29</sup> The soft-mode criterion is mathematically equivalent to a zero-eigenvalue bifurcation but does not identify Hopf bifurcations. Since none of the transitions described in this paper is Hopf, the soft-mode condition is equivalent to our dynamical instability criterion given in (53).

<sup>30</sup> P.G. Drazin, *Solitons: An Introduction* (Cambridge University Press, New York, 1989).

<sup>31</sup> P.M. Fitzpatrick, *Principles of Celestial Mechanics* (Academic Press, New York, 1970), pp. 68-77.

The first formula of Section VI should include a contribution from the driving current. In our choice of gauge,

$$E = - \sum_{\text{all}} \cos \phi_j - I \sum_{j=1}^{N+1} \phi_j^V.$$

Accordingly, Eq. (64) becomes

$$\sqrt{1 - I^2} + 2 \cos(\pi f_{\text{NV-FF}}) + I \arcsin(I) - 2 \sin(\pi f_{\text{NV-FF}})(1 - 2I^2/L)^{-1/2} - I \arcsin(\sqrt{L/2}) = 0,$$

and  $f_{\text{NV-FF}}(I = 0) = 1/3$  remains unaltered. Figure 15 is very slightly modified as shown. The conclusions do not change.

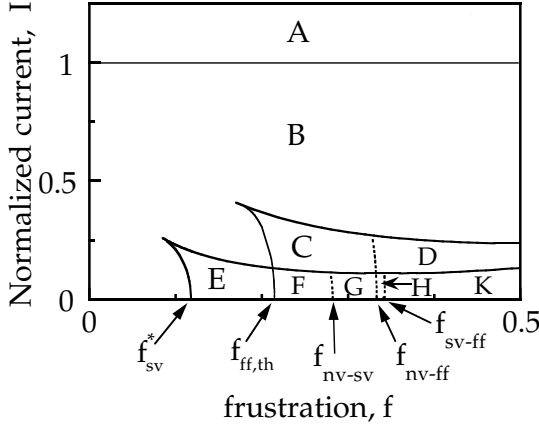


FIG. 18. (Corrected Fig. 15) Phase diagram of the NV, SV and FF solutions in the infinite (no edges) ladder—also relevant for the ring ladder. Note that region H shrinks as the number of junctions is increased (i.e.  $f_{\text{sv-ff}}$  tends asymptotically to  $f_{\text{nv-ff}}$  as  $N \rightarrow \infty$ ). Thus, the region H in the figure is only indicative.